Future Batteries 4 (2024) 100006

Contents lists available at ScienceDirect

Future Batteries

journal homepage: www.sciencedirect.com/journal/future-batteries

Diagnosis of lithium-ion batteries degradation with P2D model parameters identification: A case study on low temperature charging

G. Sordi *, M. Sedzik, A. Casalegno, C. Rabissi

Politecnico di Milano, Department of Energy, via Lambruschini 4, 20156 Milano, Italy

ARTICLE INFO

Keywords:
Lithium-ion battery
Degradation
Parameter identification
Lithium plating
Electrochemical Impedance Spectroscopy
Charging

ABSTRACT

The estimation of the state of health (SoH) of a lithium-ion battery is still a hot topic in the scientific research. This publication deals with the combined use of optimized tests, also involving impedance spectroscopy, and physical models to investigate lithium-ion batteries degradation. As a case study, this method is firstly applied on a low-temperature charging degradation campaign, in order to expectedly generate a lithium plating-dominated ageing state. Degradation tests, performed under previously selected combinations of operating conditions, are performed down to 75 % SoH on commercial samples, determining severe ageing rate up to 1.5 % capacity loss per equivalent full cycle. The proposed interpretation methodology identifies the ageing to be dominated by the loss of lithium inventory, consistently with the expected degradation mechanism. Large electrolyte consumption is also detected, which induces a strongly anisotropic utilization of the electrodes during discharge, as confirmed by pseudo-two-dimensional (P2D) model simulations. This activity contributes to verify the reliability of the methodology, elucidate the effect of lithium plating on the performance and underline the effect of the operating conditions at low temperature, paving the way to the application on real-world conditions.

Introduction

Lithium-ion batteries are spreading thanks to their high energy density and relatively low cost, especially in the field of electric vehicles and stationary energy storage. Despite the technology is already on the market, lithium-ion batteries degradation is still a hot topic at both the research and industrial levels. Different experimental techniques and modelling tools exist, all with specific pros and cons. A suitable methodology for state of heath (SoH) evaluation is needed to quantify the residual capabilities of a battery, like the driving range and maximum power delivery of an electric vehicle (EV), and to evaluate his remaining lifetime and possible re-use in a different application, such as a second-life in stationary storage systems. As reviewed in [1], SoH estimation methods are commonly divided into direct measurement, differential analysis, model-based and data-driven methods. The first two classes are more suitable for offline applications since they are time-consuming and require specific conditions like constant current measurements. However, the direct measurement provides a relevant and accurate information (usually residual capacity, sometimes residual resistance), but do not allow to infer the origin for degradation. Differential analyses enable to identify classes of mechanisms, but they do not take into account far from equilibrium behaviour (e.g. mild/high C-rate operation). Model-based methods spans from simple electrical circuit modelling to physical models. In this wide family, the simpler the model, the easier and faster the identification of its parameters and the simulation of SoH. However, the accuracy and universality of the results require complex models. For data-driven models, their limitation is the need of large amount of data and complex implementation to increase their reliability, especially for online application.

In the previous publications of the same authors [2-4], a diagnostic methodology has been developed, combining the pseudo-two-dimensional model (P2D) and an optimised sequence of tests, which shortens testing times while easing the identification of model parameters. This approach provided superior results when applied to reproduce the operation of a fresh cell, resulting reliable over a very wide set of operating conditions. The extensibility of this approach to ageing investigation is of utter interest but requires to be demonstrated. The strategy pursued for such scope is to apply the methodology to an ideally known ageing condition to verify its suitability and reliability. Lithium plating constitutes a good candidate mechanism, due to its systematic and peculiar trigger conditions, to be able to apply the methodology to an expectedly single ageing mechanism-dominated state. In the following, the fundamentals of

* Corresponding author.
E-mail address: gabriele.sordi@polimi.it (G. Sordi).

https://doi.org/10.1016/j.fub.2024.100006
Received 5 May 2024; Received in revised form 9 August 2024; Accepted 29 September 2024
Available online 5 October 2024

Nomenclature

Acronym	*Description*
CC	Constant current
CV	Constant Voltage
D1	First discharge of the developed diagnostic protocol (see Section 2.2.3)
D2	Second discharge of the developed diagnostic protocol (see Section 2.2.3)
DC	Direct Current
DoC	Depth of Charge
DV	Differential Voltage
E1	First EIS of the developed diagnostic protocol (see Section 2.2.3)
E2	Second EIS of the developed diagnostic protocol (see Section 2.2.3)
EFC	Equivalent Full Cycle
EIS	Electrochemical Impedance Spectroscopy
EV	Electric Vehicle
HFR	High Frequency Resistance
ICP-OES	Inductively Coupled Plasma – Optical Emission Spectroscopy
LAM	Loss of Active electrode Material
LFP	Lithium iron phosphate battery
LLI	Loss of Lithium Inventory
LMO	Lithium-manganese-oxide battery
NMC	Lithium-nickel-manganese-cobalt-oxide battery
OCP	Open Circuit Potential
OCV	Open Circuit Voltage
P2D	Pseudo Two-Dimensional Model
PSO	Particle Swarm Optimisation
R	Relaxation of the developed diagnostic protocol (see Section 2.2.3)
SEI	Solid Electrolyte Interphase
SoC	State of Charge
SoH	State of Health

Latin

A_c	$[m^2]$, Cross section area
c	$[mol \times m^{-3}]$, Lithium concentration
C_{dl}	$[F \times m^{-2}]$, Double layer capacitance
D	$[m^2 \times s^{-1}]$, Lithium diffusion coefficient
E	$[V]$, Equilibrium potential
F	$[A \times s \times mol^{-1}]$, Faraday constant
$HFR_{\exp}$	$[\Omega]$, Experimental High Frequency Resistance
I	$[A]$, Total current
K_1	$[-]$, Scaling factor for electrolyte resistance estimation
K_2	$[-]$, Scaling factor for film resistance estimation.
L	$[m]$, Cell component length
OCV	$[V]$, Open Circuit Voltage
Q	$[mAh]$, Capacity
R_{eq}	$[\Omega]$, Lumped battery resistance
R_{cuc}	$[\Omega]$, Current collectors resistance
R_{film}	$[\Omega \times m^2]$, Film resistance
x_{Li}	$[-]$, Lithium molar fraction
ΔV	$[V]$, Cell voltage

Greek

ε	$[-]$, Material fraction
σ_{el}	$[S \times m^{-1}]$, Electrolyte ionic conductivity

Subscript and Superscript

$_{\max}$	maximum
$_n$	negative
$_p$	positive
$_s$	solid
$_{tot}$	total
aged	Aged
$_{BoL}$	Begin of life

lithium plating and its detection techniques are reviewed to assess its interesting features considering the scope of this work.

Lithium plating mechanism

Lithium plating is the deposition of lithium in metal phase on the surface of graphitic electrodes. It can occur in parallel to the usual lithium intercalation into graphite, due to specific operating conditions. There are two possible paths, which can occur at the same time [5–8].

The first is the charge-transfer limitation: during a charge, lithium-ions can undergo the following reaction

$$Li^+ + e^- \rightarrow Li \tag{1}$$

because the potential at the negative electrode falls below 0 V vs Li^+/Li, triggering the reaction [7,9,10]. Both lithium intercalation and lithium deposition can take place and they are in competition, resulting in a mixed potential case. The relationships between plating and operating conditions have been investigated in [11,12]. In general terms, it is favoured by low temperature, high charging current and high voltage/state of charge [5,7,13,14]. As a matter of fact,

- **low temperatures** worsen the kinetics of the reactions and the conductive properties of the materials, increasing the overpotentials and, thus, lowering the electrode potential, which can reach 0 V vs Li/Li^+;
- similarly, **high charging currents** induce large overpotentials, while aged cells can have worse conductive properties or lower active surface due to degradation, which favour high overpotentials, too;
- lastly, **high state of charge** (SoC) is associated with low equilibrium potential at the negative electrode, which is close to 0 V. Therefore, lower overpotentials are enough to trigger lithium plating at high SoC.

In addition to the charge-transfer limitation, the second mechanism is the solid-diffusion limitation. During a charge, lithium concentration on the surface of the graphite can approach the maximum value. If the lithium diffusion rate in the solid electrode, from surface to bulk, is lower than the rate of lithium transport in the electrolyte, lithium starts to deposit on the surface as plated lithium [7,9]. Also for this path:

- since solid diffusivity is well-known to follow an Arrhenius relation [15], **low temperature** favours lithium plating due to a further reduced intercalation rate;
- **high charging current** induce heterogeneous utilization of the electrode up to a mass-transport limited condition, so that lithium can saturate the active sites locally;
- **high SoC** are characterized by high lithiation degrees in graphite, thus the occurrence of saturation of particle surface is facilitated in presence of lithium diffusion limitations;

- **aged cells** are more prone to this condition, too [6], likely featuring a decrease of transport properties of active materials;
- Moreover, the presence of local defects, ill-connected particles or non-uniformity in the electrode structure can lead to lithium plating locally [6,7].

Lithium plating is in principle a reversible process. As it forms electrochemically, during the subsequent discharge process lithium can react with electrons and become ion again, taking part in the normal cycling operation. The backward reaction Li/Li^{+} is named lithium stripping. However, during the discharge process a portion of plated lithium typically loses the electric contact with the conductive electrode matrix, becoming electrically isolated, resulting in capacity loss [5,6].

Lithium metal deposition is the most notable degradation mechanism at low temperatures. However, due to degradation plating can manifest also at mild operating conditions and even becoming the dominant ageing mechanism, inducing an acceleration of the degradation rate of the battery, switching from linear to nonlinear [13]. Moreover, it is the limiting phenomenon to fast charging, forcing the research towards optimised plating-free charging profiles [16]. Lithium plating leads to severe performance degradation and safety issues. The plated lithium favours the growth of lithium dendrites, especially at high current densities: the dendrites grow rapidly and, if they pierce the separator and connect the electrodes electrically, it results in an internal short circuit [5,17]. The plated lithium may also react with the electrolyte, causing the solid electrolyte interphase (SEI) layer to grow [14]: as a result, SEI resistance and cell impedance increase [6,18]. Deposited Li metal can also intercalate, both electrochemically and chemically [14].

Analysis of voltage relaxation after a charge

The investigation of lithium plating has been performed in different ways:

- starting from the mixed potential of lithium stripping during relaxation or slow discharge right after a charging process both in half cell [19] or full cell [20] configuration,
- by means of electrochemical impedance spectroscopy (EIS) [20],
- on the discharge curve [21] as loss of active graphite material at delithiated state or from peak-to-peak distance change [11],
- as an additional peak on the incremental capacity during high C-rate charge [22],
- with a C-rate plateau during the constant-voltage (CV) phase during charge [23]
- by means of post-mortem analysis [24,25].

A summary of several relevant scientific researches is reported in Table 1. Lithium plating is usually promoted by low temperature and high C-rate/SoC during charge phase, inducing relevant loss of lithium inventory and increase of impedance.

Among all the techniques, the analysis of the voltage evolution after a charge is one diagnostic technique for lithium plating [8,14,27]. Among its pros, it does not require particular and expensive equipment and it is non-destructive. In the literature, it is usually applied on lithium iron phosphate (LFP) cells, because the evolution of the cathode during low-temperature operation can be considered negligible [5] and the open-circuit potential (OCP) of the material is so flat that it can be considered as a reference electrode [28]. This technique is a modification of the usual differential voltage (DV) analysis applied on discharges at low C-rates. In this case, it exploits the derivative of voltage with respect to time during the relaxation transient after a charge step [27]. It is an indirect measure of plating, since it traces back the lithium that has plated previously, by analysing the voltage trend related to the following lithium stripping process. Indeed, when plating occurs, lithium is deposited over the surface of graphite. At the end of the charge step, plated lithium is electrochemically active. Since no load is applied to the ends of the battery, the system tends to an equilibrium state and all the gradients tend to zero, with the relative time constants of the phenomena. Plated lithium undergoes the stripping reaction in parallel to the normal deintercalation, that is a mixed potential condition [14]. The occurrence of the mixed potential condition is associated with a specific voltage trend over time (Fig. 3a). Indeed, the most common trend of relaxation is a decreasing exponential, while the mixed potential condition involves the formation of a voltage plateau [8]. When the mixed potential condition is over, there is an evident change of derivative over time, which can be magnified by performing the derivative of voltage over time or vice versa, highlighting a peak or valley (Fig. 3b-c). It is known in the literature that lithium stripping reaction is favoured over lithium deintercalation [29], thus it is expected to stop earlier than lithium deintercalation reaction. As a result, the end of the mixed potential area is associated with the end of the stripping process.

Furthermore, the time duration of this voltage plateau is correlated to the magnitude of the stripped lithium, which, in turn, is related to the amount of plated lithium in the preceding charge [14]. Indeed, Von Lüders, Zinth et al. investigated lithium plating at $-20\,^{\circ}C$ [26] and $-2\,^{\circ}C$ [14] on lithium-nickel-manganese-cobalt oxide (NMC)|Graphite cells with in-situ neutron diffraction. They monitored lithium plating indirectly through the reflections of the lithium graphite phases. They observed that the amount of plated lithium correlates nonlinearly with the charging C-rate. Moreover, they compared the diffraction data with the voltage relaxation and found a good agreement. They observed that the rate of intercalation of reversibly deposited lithium seems independent of the amount of deposited lithium itself, which allows to state that the duration of the mixed potential plateau is an indicator of the amount of plated lithium in the preceding charge.

As emerges from this brief literature review, lithium plating appears an optimal candidate for this work, since it proves to be always the dominant mechanism at sub-zero temperatures. Moreover, to the authors knowledge, literature on lithium plating lacks holistic methodologies aiming to its physical-based investigation, which could be performed by quantifying physical parameters evolution.

In this work, the diagnostic methodology outlined in [2], combining experimental and physical modelling approach, is extended to aged cells to demonstrate a novel SoH estimation tool, enabling a physically-sound distinction and quantification of the several degradation mechanisms involved with battery operation, with a holistic approach. Such a tool is lacking in the literature and very much needed for the sake of degradation understanding and durability optimization of the technology. It is hereby demonstrated by applying it to plating-dominated ageing, which is appositely promoted through low-temperature charging stress tests.

The methodology relies on exploiting a selected combination of several high-sensitivity measurement techniques performed at specific operating conditions, to maximize P2D model sensitivity over a set of meaningful physical parameters. Such a wide combination of conditions and techniques, which enables to reach a physically consistent solution, will be challenged against the expected ageing mechanism. Also, it will be adopted to identify the impact of operating stressors (such as depth of charge, temperature, average soc, charging C-rate) to characterize the impact of such parameters in a physically-sound perspective.

The structure of this paper is as follows. Section 2 describes the samples, the experimental campaigns and the diagnostic tools. In Section 3, the results of the pulses campaign are reported, while Section 4 discusses the results of the cycling campaign with the support of the models.

Methodology

In this section, the methodology of the analysis is described. First, the main information regarding the battery sample and testing equipment is summarized. Then, the experimental campaigns are outlined, together with the characterization procedure to quantify the residual capabilities

Table 1
Summary of research articles on lithium plating.

Authors	Chemistry	Method	Temp	Result
Von Lüders et al.[14], Zinth et al.[26]	NMC| Graphite	In-situ neutron diffraction compared with relaxation data	−20 °C; −2 °C	• Amount of plated lithium correlates nonlinearly with the charging C-rate • Good agreement between neutron diffraction and voltage relaxation • Intercalation rate of reversibly deposited lithium seems independent of the amount of deposited lithium itself
Schindler et al.[27]	LFP| Graphite	Voltage relaxation analysis with superimposed EIS	−5 °C; −15 °C; −25 °C	Two main features related to the onset of lithium plating (particularly strong where large lithium deposition was identified through the differential voltage method): • a decrease of the high frequency resistance • shrinking of the arc of the negative electrode charge transfer process. Limitation: such use of EIS during thermal transient promotes battery self-heating during charge, affecting the kinetics and material properties, requiring a reliable thermal model to elucidate and separate this effect.
Petzl et al.[5]	LFP| Graphite	• Differential analysis of C/10 charge and discharge • Capacity test with 1C charge and discharge • EIS • Cell opening in glovebox to estimate the amount of plated lithium	−22 °C	Differential analysis: • Identified large loss of lithium inventory, causing electrodes imbalance. • LLI in turn limits a further occurrence of lithium plating, since the first stage of graphite, characterized by low OCP, becomes more and more inaccessible. This effect leads to a stabilization of capacity loss. EIS: • an increase of the high frequency impedance, relating this feature to a significantly reduced ionic conductivity of the electrolyte, which underwent side reactions with deposited lithium, forming surface films that increase the cell impedance. • High frequency resistance resembles the stabilization of the capacity loss, thus they are likely to be correlated. Cell opening: • Lithium plating observed at all ageing states through water contact. • Formation of a flat and uniform silver layer is observed after 80 cycles, corresponding to lithium plating, differently from the grey colour of graphite. • Increasingly dry electrode with ageing, supporting the interpretation of electrolyte consumption. • Thickness and mass measurements further corroborated their analyses.
Ecker et al.[6]	NMC| Graphite LFP| Graphite	• 1C discharge curve • Differential analysis of C/25 discharge • EIS • Pulse test • Inductively Coupled Plasma – Optical Emission Spectroscopy (ICP-OES) • Porosimetry, thickness and weight measurements.	−10 °C; 0 °C; 10 °C	Discharge and differential analysis • Dominant role of temperature • Plating occurs at a relevant extent only at high end-of-charge SoC with high depth of charge due to large concentration gradients in the cell. • Strong capacity loss rate • Loss of lithium inventory and graphite active EIS and pulses • Increase of the high frequency resistance and of the charge-transfer arc and an increase of the direct current (DC) resistance. Post-mortem analyses: confirm lithium plating as origin of degradation. Limitation: the authors stated how a generalization of the trends is very hard due to many different design strategies, but the dominant role of temperature is confirmed.

of the cells. Two experimental campaigns are performed: one charging pulses campaign and a cycling campaign. Lastly, physical models are described and the method for the identification of their parameters is reported. Two models are exploited: the P2D model and one equilibrium model. The equilibrium model is reported in detail since it is appositely developed for the purpose of this analysis.

With respect to previous works of the same authors, the approach is here extended to aged cells. The parameter identification procedure was originally developed to reproduce the operation of a fresh cell and it is here applied successfully for the first time to simulate the behavior of increasingly aged cells. At the same time, the choice of the fitting parameters has been updated to include the thermodynamic parameters of the equilibrium model and to take into account degradation mechanisms. Regarding the characterization procedure, the combined use of discharges and EIS is in common with previous works, but a C/10 discharge is here added to enable the estimation of thermodynamic parameters. More detailed information is available in the next sections.

Battery samples and testbench

The characteristics of the tested samples are listed in Table 2. The positive electrode is a blend of NMC and lithium-manganese oxide (LMO). All samples were pristine. No information regarding electrolyte and binder composition is available.

The experimental setup consists of a custom-developed testing station, which includes a single power supply (NI RMX-4124) and a five-channels electronic load (Chroma UM 63640–80–80) with high-speed acquisition. The system results in four independent testing channels with EIS capabilities. All tests are performed in a Binder MKF 720 Eucar 6 climatic chamber, capable of $-40\ ^{\circ}C\ /\ +180\ ^{\circ}C$ testing. Test temperature always refers to the thermal chamber setpoint. Moreover, cell experiences self-heating, which is monitored by means of type K thermocouples, attached to the surface of each sample, in order to acquire its temperature by way of a NI CDAQ-9211 temperature acquisition board. The test bench is connected controlled with a custom LabView©-coded workspace, recording voltage, current and temperature data with a 2 Hz frequency and monitoring the batteries operating conditions to be within the safety limits.

For any further detail, the reader is addressed to [4].

Experimental campaigns

Low temperature pulses

This campaign aims at understanding the role of the operating conditions at very low temperature, where the lithium plating phenomenon is expected to be promoted. This campaign tries to verify the occurrence of lithium plating exploiting the analysis of the voltage trend in the relaxation that follows a low temperature charge, explained in Section 1. This technique is suitable for the purpose, since it is non-destructive, easy to implement, relatively fast and it is very sensitive and specific to lithium plating.

The complete experimental procedure is reported in Fig. 1. Starting from 100 %, cells are discharged down to the prescribed SoC level. After a 5 h resting period to reach equilibrium, a pulse with conditions listed in Table 3 is applied and, when the charge phase is over, relaxation is monitored for 5 h. If voltage hits the maximum voltage limit, CV phase is performed until the desired depth of charge (DoC) is achieved.

Table 2
Characteristics of the experimental samples [30].

Property	Value
Manufacturer	SONY
Model	US18650V3
Nominal capacity	2.25 Ah
Voltage cut-offs	2.5V–4.2 V
Electrode materials	Graphite|NMC+LMO
Continuous max charge C-rate	1C

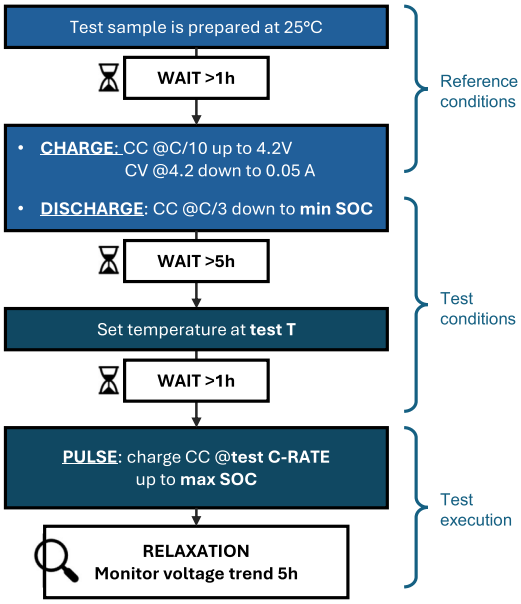

Fig. 1. Flowchart of experimental procedure to perform pulses.

Preliminary tests were conducted to identify a meaningful selection of operating conditions, hereby only the final results are showed. Different cells at pristine conditions are employed, since these conditions are so severe that few repetitions induce significant ageing, as discussed in the next sections.

Low temperature cycling campaign

After the study of the operating conditions performed through pulses, a degradation campaign is conducted to identify their effect on ageing and performance. The operating conditions are reported in Table 4, which are a subset of the ones of the pulses campaign. Each cycling condition was applied on a different cell. All the cells are discharged at C/5: the equal C-rate enables to state that all the differences between the cycles are due to the charge phase, where lithium plating is expected. Moreover, C/5 is a low C-rate, which is not believed to induce significant degradation. A total of 8 cells are tested. Test A10 (50 %–80 % SoC, 1C charge, $-10\ ^{\circ}C$) is usually considered as reference cycle.

Table 3
Experimental matrix of the low temperature pulses campaign. Colours ease the comparability of operating conditions.

#	Label	T [°C]	Min SoC [%]	Max SoC [%]	Depth of charge [%]	Charge C-rate [-]
1	A5+	5	50	80	30	1
2	B5+					0.5
3	C5+		30	60		1
4	D5+				50	
5	A0	0	50	80	30	
6	B0					0.5
7	C0		30	60		1
8	D0				50	
9	A5	-5	50	80	30	
10	B5					0.5
11	C5		30	60		1
12	D5				50	
13	A10	-10	50	80	30	
14	B10					0.5
15	C10		30	60		1
16	D10			80	50	

Table 4
Experimental matrix of the low temperature cycling campaign.

#	Label	T [°C]	Min SoC [%]	Max SoC [%]	Depth of charge [%]	Charge C-rate [-]
1	A0	0	50	80	30	1
2	B0					0.5
3	C0		30	60		1
4	D0				50	
5	A10	-10	50	80	30	0.5
6	B10					
7	C10		30	60		1
8	D10			80	50	

The experimental matrix is structured so that the effect of four operating conditions is analysed, as highlighted by the coloured table, with two values for each variable:

- Temperature: −10 °C and 0 °C
- Charging C-rate: 1C and C/2
- Depth of charge: 30 % and 50 %
- State of charge window: minimum SoC 50 % or 30 %, maximum SoC 80 % or 60 %.

As for the pulses campaign, before cycling, the cell is firstly charged to SoC 100 % at 25 °C with constant current (CC) of C/10 up to 4.2 V, followed by a CV phase until the current drops below 0.05 A (Fig. 1). After that, it is discharged with coulomb-counting at C/3 down to the minimum SoC swept by the cycle. The SoC is defined with respect to the nominal case, also for an aged cell (e.g. SoC 30 % requires a 70 % discharge after the full charge step, which corresponds to 1.575 Ah discharge capacity). The chamber temperature is then brought to the desired temperature and, after at least 1 h of attempering, the cycles start again with the charge phase.

Fig. 2 shows how cycles are performed. The first two cycles are performed, with coulomb counting to guarantee the desired DoC. If the voltage hits the upper cut-off limit, the cycle proceeds with CV phase until the charge throughput achieves the desired value. After the second cycle, the following ones are voltage-controlled: the same voltage and current thresholds that were obtained for cycle 2 are applied to all the following cycles. As a result, after cycle 2 the DoC might be different

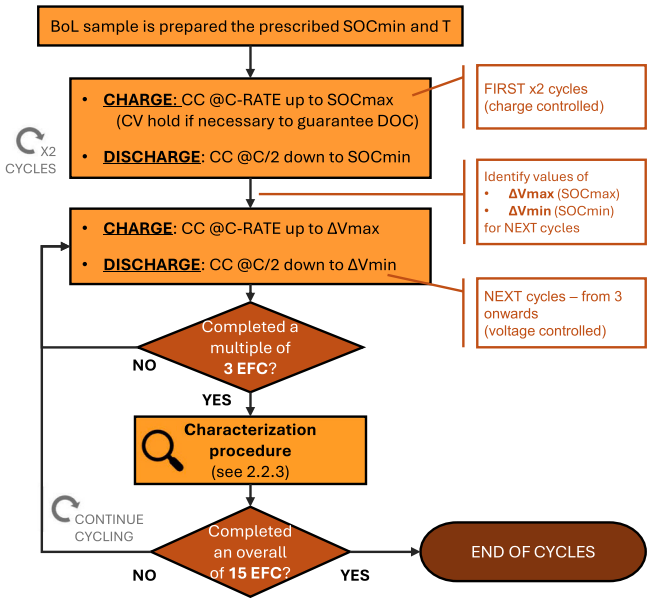

Fig. 2. Flowchart of experimental procedure to perform cycles.

from the nominal one due to degradation. The campaign is interrupted every 3 equivalent full cycles (EFCs) to perform the periodic characterization procedure. A total of 15 EFC is carried out for each cell. The campaign was performed as a continued sequence of cycles and characterization procedures until 12 EFC. After that, an interruption of around one month occurred. The last 3 EFC were later performed.

Characterization procedure

Cycled cells undergo a characterization procedure every 3 EFC. It consists of one full discharge at C/10 and 25 °C and an optimized sequence of tests, whose development was described in [2], constituted by:

- (E1) EIS test on the battery at 10 °C and 100 % SoC with 40 logarithmically spaced frequencies in the range 4000Hz-0.01 Hz;
- (D1) discharge at 10 °C and 2C from 100 % SoC to 50 % SoC;
- (R) a relaxation of 1000 s. After that, the climate chamber temperature is set equal to 25 °C and, when the thermal transient is over, an (E2) EIS within the same frequency interval of the first one is performed;
- (D2) the battery is discharged at 25 °C and 1C from 50 % SoC until the lower voltage limit is reached (theoretical depth of discharge is 50 %).

State of charge is always computed in nominal terms, without rescaling to the residual capacity. These curves are later fed as input information to identify the physical parameters of the model through a parameters identification procedure described in Section 2.5.

P2D model

The P2D model [3], implemented in COMSOL Multiphysics®, is exploited to support the interpretation by identifying the value of a selected set of kinetic and mass transport-related parameters, listed in Section 2.5, by reproducing tests D1, D2, E1, E2 of the characterisation procedure described in Section 2.2.3. The model accounts for lithium transport in the electrolyte and in the electrodes-bulk phase (which is represented as a sequence of spherical particles), the electrochemical reaction on the surface of the electrodes by means of the Butler-Volmer equation and electron conduction in the electrode. Moreover, it solves double layer (dis/)charging on the surface of both electrodes, the resistance of current collectors and other internal connections [2] and surface layers like SEI are modelled as lumped resistances. Double layers are implemented as an additional current density, in parallel to that of the electrochemical reaction, on the surface of electrode particles, as in [31]. It depends on the capacitance (property of the layer, constant and uniform) and the overpotential at the electrode-electrolyte interphase. Film resistances are modelled as ohmic 0D resistance on the surface of the particles, inducing an ohmic drop at the electrode-electrolyte interphase.

The model embeds a 2D thermal model [4] to account for internal heat generation and the convection with surrounding ambient air. It calculates the internal temperature distribution at each time-step resulting from the P2D model heat generation. The averaged internal temperature is then adopted to correct the value of diffusive and kinetics properties, following an Arrhenius relation.

EIS is also modelled with the P2D model in the time domain or frequency domain, by simulating the voltage response of the cell consequent to a sinusoidal perturbation of current, at varying frequency.

Equilibrium model

Additionally, a quasi-equilibrium model is hereby developed in Matlab® environment to support the interpretation of state of health and it is included in the modelling framework. The purpose is the simulation of C/10 discharge curves, considered as close-to-equilibrium

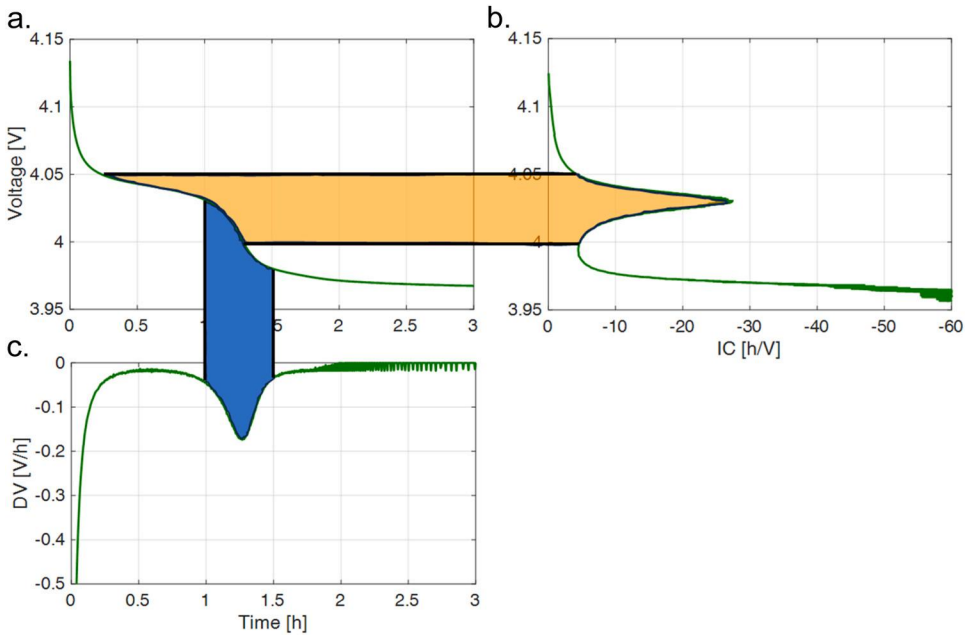

Fig. 3. Example of cell voltage evolution during experimental relaxation test after one charge pulse. (a) Voltage over time, (b) derivative of time with respect to voltage and (c) derivative of voltage with respect to time.

conditions. Therefore, the model is a 0D, equilibrium model. No kinetic or mass transport losses are included, other than a lumped ohmic resistance R_{eq}. Indeed, battery voltage ΔV is computed as

$$\Delta V = \quad E_p - E_n - I^{*}R_{eq} \tag{2}$$

where E_p is the positive electrode open circuit potential, E_n the negative electrode OCP and I the total applied current. OCP curves are taken as look-up tables as function of the lithium molar fraction and were directly measured in coin cell setup. In the present case, R_{eq} is estimated equal to 0.151mΩ with a pulse test.

Battery ageing at equilibrium condition is described through three degradation parameters, namely loss of lithium inventory (LLI) and loss of active electrode material (LAM) of both electrodes, as common practice in the literature. LLI describes all the degradation phenomena involving a loss of cyclable lithium, without affecting the structure of the electrodes. On the other hand, LAM refers to the degradation of the electrodes, so that their capability of accepting charge decreases. In this model, LAM is considered as purely delithiated, meaning that no loss of lithium is induced by the degradation of the electrodes. Despite the positive electrode is a blend, one LAM_p parameter and a single OCP curve are present.

Indeed, the total charge inside the battery Q_i^j in a general ageing state j is computed as the sum of the charge which is stored in the electrodes:

$$Q_{tot}^j = Q_p^j + Q_n^j \tag{3}$$

The amount of charge in the electrode i is computed as the multiplication of its value at fresh state Q_i^{BoL} and the remaining usable fraction:

$$Q_i^j = Q_i^{BoL}{}^{*}\left(1 - LAM_i^j\right) \tag{4}$$

The fresh quantity is quantified depending on the geometry and the lithiation level, as follows:

$$Q_i^{BoL} = A_c{}^{*}F^{*}(L_i{}^{*}\varepsilon_{s,i}{}^{*}c_{s,\max,i}{}^{*}x_{Li,i}) \tag{5}$$

where A_c is the cross-section area, F is the Faraday constant, L_i is the electrode thickness, $\varepsilon_{s,i}$ the solid volume fraction of the electrode and $x_{Li,i}$ lithium molar fraction hosted in the electrode. This equation is valid at all battery SoCs. Due to a LLI degradation mechanism, the total battery charge decreases, so that the following equation holds true:

$$Q_{tot}^j = Q_{tot}^{BoL}{}^{*}(1 - LLI^j) \tag{6}$$

As a result, the lithium molar fractions in the electrodes at SoC 100 % and 0 % would change. In order to define the SoC 100 % conditions of the electrodes for an aged cell, a nonlinear problem is solved through *fsolve* function in Matlab®, giving the following set of constrains:

$$E_p - E_n = OCV \tag{7}$$

$$Q_p^{aged}\left(x_{Li,p}\right) + Q_n^{aged}\left(x_{Li,n}\right) = Q_{tot}^{aged} \tag{8}$$

$$E_p = E_p\left(x_{Li,p}\right) \tag{9}$$

$$E_n = E_n\left(x_{Li,n}\right) \tag{10}$$

Where Q_p^{aged} and Q_n^{aged} depend on LAMp and LAMn as in Eq. 4 and Q_{tot}^{aged} on LLI as in Eq. 6. Therefore, the target cell voltage at rest OCV is achieved by splitting the charge between the electrodes so that both the desired voltage value, which depends on the lithium content in the electrodes, is obtained and the conservation of the total amount of charge in the battery is ensured.

The same equations are present in the P2D model, but this simplified model is developed to simulate low C-rate discharge, to save computation time. A sensitivity analysis of the parameters effect is reported in Section S1 of the Supplementary Materials.

The lithium molar fraction at battery SoC 100 % and 0 % for the cells under investigation at fresh state are reported in Table 5. Other than these parameters, the model requires electrodes thickness and solid fractions as well as the cross-section area as input parameters.

Table 5
Lithium molar fractions at SoC 100 % and 0 % for a fresh cell, estimating from the best fit OCPs derived in coin cell configuration.

Battery SoC	Negative electrode	Positive electrode
100 %	0.9050	0.4213
0 %	0.0158	0.9674

Parameter identification procedure

In this section, the parameter identification procedure is outlined (with reference to the characterization procedure of Section 2.2.3).

- Step 1: first, the thermodynamic parameters are estimated through the full discharge at 25 °C C/10, under the assumption of close-to-equilibrium. The description of the algorithm is reported in Section S2 of the Supplementary Materials. The equilibrium model (described in Section 2.4) is exploited in this step, while the followings refer to the P2D model.
- Step 2: after that, the kinetic and mass transport parameters are computed with a stepwise procedure, similar to the one described in [2] for fresh cells. The model is calibrated against the two impedance spectra (E1) and (E2) simultaneously, by optimizing kinetic constants ($k_{p,0}$, $k_{n,0}$) and the double layer capacitance of the positive electrode, $C_{dl,p}$. 8 frequencies in the 4000Hz-1Hz frequency range are selected. Other parameters are fixed to an intermediate value in the literature range as first guess. Since solid diffusivities and, at a certain extent, electrolyte properties have a minor effect on EIS, this solution is viable and will be corroborated with Step 4. In this step, the high frequency resistance (HFR) value, e.g. the first intercept of the spectra with the Real(Z) axis with null imaginary part, is subtracted to the real part of the impedance at all frequencies. In this way, only the charge transfer resistance is considered.
- Step 3: solid diffusivities ($D_{s,p,0}$, $D_{s,n,0}$) and electrolyte conductivity (σ_{el}) are identified through the minimization of differences between model and experimental partial discharges (D1) and (D2). The current collector resistance is assumed to be constant and equal to the BOL value. This hypothesis is equivalent to neglect their corrosion, which is assumed to be limited according to the safe operating conditions at which the cells are operated. On the contrary, SEI layer is expected to grow throughout the campaigns. Therefore, its resistance $R_{film,n}$ is estimated according to the following equation:

$$R_{film,n} = (HFR_{exp} - R_{cuc} - R_0 - R_{el})*K_2 \quad (11)$$

where HFR_{exp} is the HFR value measured at 25 °C, 50 % SoC of the aged cell. Current collector resistance, R_{cuc}, and the sum of other resistances, like electronic resistance of the electrodes, R_0, are equal to the value of the fresh cell. In practice, R_0 is the modelled cell resistance at the same operating conditions, but with the electrolyte conductivity σ_{el} equal to 1000 S/m and R_{cuc} equal to zero, thus negligible contributions of electrolyte and current collectors. R_{el} is the contribution of the electrolyte conductivity to the cell resistance, computed as

$$R_{el} = \frac{K_1}{\sigma_{el}} \quad (12)$$

the ratio between a constant K_1 and the electrolyte conductivity. Lastly, the K_2 parameter is a scaling factor, which takes into account the active area of the electrode and the current distribution inside the thickness of the negative electrode. It is estimated equal to 0.3664.

- Step 4: finally, Step 2 is repeated employing solid diffusivities and electrolyte conductivity values that were identified in Step 3. In this step, the interval of variability of the kinetic rate constants is slightly shrunk and centred on the solution of Step 2, in order to better investigate the solution space.

For all the steps, parameters value is identified by means of a particle swarm optimisation (PSO) algorithm. The algorithm attempts at minimising a cost function, different for each step. The identified solution is the set of optimal values for each investigated parameter with a confidence band. This confidence band is the interval of variation for each parameter. It is derived by all the solutions leading to an increased cost function up to 5 % with respect to the optimal one. Indeed, since model simulations never perfectly overlap with experimental data, a confidence band is here added to provide a more realistic estimation of physical parameters and to identify whether the trend of one parameter due to battery ageing is meaningful or not. If confidence band is little, the value of the parameter is well defined. On the contrary, wide confidence bands refer to parameters which are hardly identifiable, and so usually less relevant for the analysis because they affect model simulations at a limited extent. More details on this representation are reported in Section S2.4 of the Supplementary Materials.

Results of the pulses campaign

One example of relaxation recorded during an experiment after a charge step is reported in Fig. 3a for pulse A10 (50 %−80 % SoC, 1C charge, −10 °C). Time zero is the instant of end of charge. As already explained in Section 1, it shows an initial quick drop, followed by a plateau, which then proceeds with the usual exponential decay, down to a stabilization value equal to the open-circuit voltage (OCV). This profile is believed to be associated to the mixed potential condition, due to concurrent occurrence of lithium intercalation and plating [14]. Fig. 3b and Fig. 3c show the derivative analysis of time with respect to voltage and vice versa, respectively. Data are processed with a Gaussian filter [32] as for the DV analysis of low-rate discharge, filtering raw data to obtain the derivatives. Coloured areas enable to highlight that the first approach magnifies the plateau region, where lithium stripping is taking place: the more time spent in the mixed potential condition, the more intense the peak is. Differently, the second approach magnifies the end condition, when all the lithium has been stripped. In the following, the second method is extensively exploited, since it is easier to visualize the amount of plated lithium as the peak position rather than as its integral.

Effect of temperature

Operating conditions are investigated one at a time. Temperature is first taken into account in Fig. 4. All pulses of type A (50 %−80 % SoC, 1C charge) are reported. Due to a technical problem in setting the SoC before performing the pulse, some tests were not executed at the exact SoC (−5 °C in the case of Fig. 4). The depth of charge is preserved, and this minor error is assumed not to bias the results at a significant extent. However, this is evident in the stabilization value of voltage in Fig. 4, a where the relaxation at −5 °C approaches a lower OCV.

The onset of a plateau is easily detectable at subzero temperatures, while it appears only slightly at higher ones. By performing the derivative, a clear peak is showed in Fig. 4b. This method highlights the presence of a mixed potential region also at 0 °C and 5 °C, hardly visible from the simple voltage curve. There is no major difference between these two temperatures, suggesting that the phenomenon might occur only in few spots, possibly close to the tab where the local current density is high [7]. Moving to lower temperatures, the peak become more evident and shifts to longer timescales. This trend is in agreement with the expectations from the literature review, where lower temperatures enhance the probability of plating, which can be present in different areas of the roll and in larger quantities [6,7]. The larger amount is translated into a longer duration of the mixed potential condition, thus a later occurrence of the peak [14]. This trend is shared by all the four combinations of pulses. As a proof, one further example is reported in Fig. 4c-d for pulse D (30 %−80 % SoC, 1C charge). The differences due to C-rate, SoC and DoC are investigated in the following paragraphs.

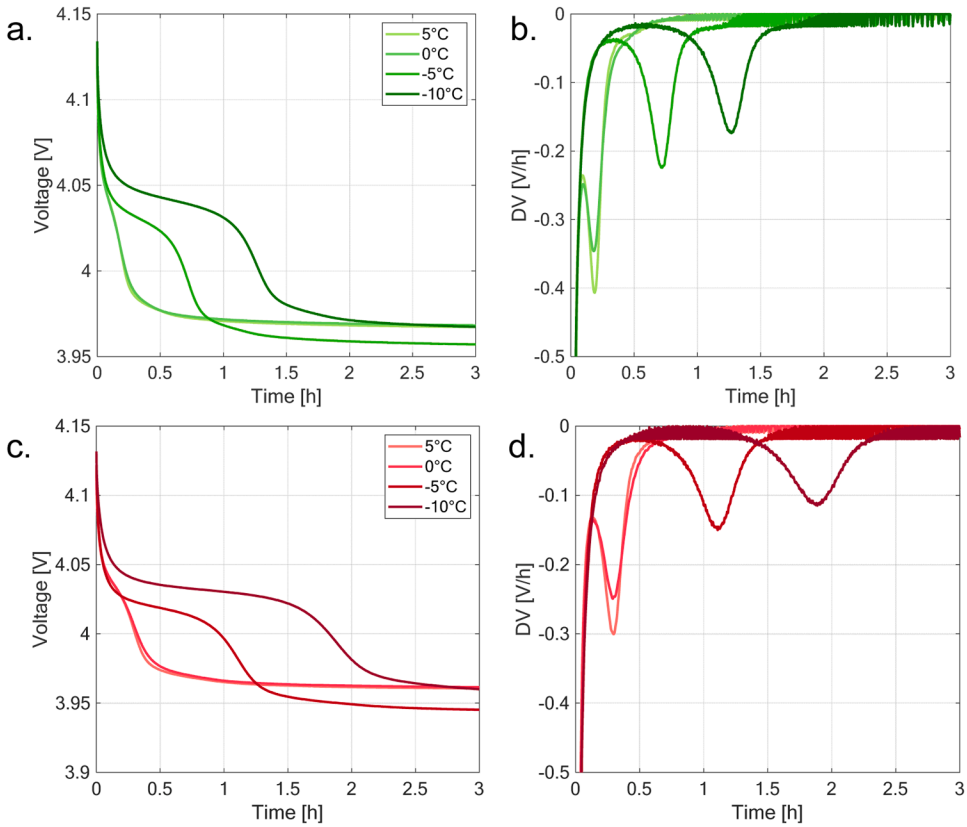

Fig. 4. Temperature effect for type A pulses (50 %−80 % SoC, 1C charge): (a) measured cell voltage evolution and (b) corresponding DV.

Effect of charging C-rate

The charging C-rate is now investigated. Type A (1C charge pulse) and B (C/2 charge pulse) at 0 °C and −10 °C are considered and reported in Fig. 5a-b. There is a clear difference between the selected C-rates, as expected from the literature review [14]. No peak is detected at 0 °C for C/2 charge, while it was distinguishable already at 5 °C for 1C charge. Indeed, the voltage shows the usual exponential decay over time, indicating that if any plating is occurring, it is at a very limited extent. At −10 °C the peak is sharp and the mixed potential region lasts for 45 min after the end of charge. Though the phenomenon increases, it is still limited with respect to the 1C case, where lithium stripping lasts for 75 min

Temperature effect for type D pulses (30 %−80 % SoC, 1C charge): (c) measured cell voltage evolution and (d) corresponding DV.

Effect of SoC and DoC

Similar analyses are briefly summarized for maximum SoC and depth of charge. The first is reported in Fig. 5c-d. No peak is detected at 0 °C for the pulse type C (30 %−60 % SoC), while at −10 °C a sharp peak appears, associated to a large plated amount, but lower than the reference case.

The peculiar characteristic of the 30 %−60 % SoC, −10 °C pulse is the appearance of a second smaller peak around 75 min. No literature was found regarding this feature, which is shared only by the same pulse carried out at −5 °C. It is assumed that this condition is due to the staging behaviour of graphite: at SoC 60 %, with large gradients originated during the pulse, the graphitic electrode is partially lithiated in the first and partially in the second stage of graphite. Therefore, the mixed condition has two timescales: during the first period, plated lithium is likely to intercalate into stage 1 of graphite, whose OCP is around 80 mV, promoting lithium reduction. When this condition is over, there is a potential drop of around 50 mV, then the mixed potential condition continues with the competition with lithium stripping and intercalation into stage 2. This feature is not observed in all the other pulses since the electrode lithiation is beyond 50 % (i.e. first stage of graphite) also locally at SoC 80 %. In this perspective, the relative position in time of both peaks is an indirect measure of the heterogeneous lithiation of the electrode. As a result, the duration of the mixed potential of pulse A and C are comparable, so they are expected to induce a similar extent of lithium plating.

Lastly, 50 % DoC shows a larger amount of plated lithium at both temperatures with respect to the 30 % case (Fig. 5e-f), consistent with larger gradients that have established during the pulse, as expected.

Mixed potential region vs temperature

As a final observation, Fig. 6 reports the position of the peak of the DV against the chamber temperature for all the pulses. A value equal to 0 is reported for pulses which do not show any peak, while for pulses of type C the time corresponding to the second, small peak is selected. Even though the number of tested conditions is limited, from 0 °C downwards it seems that the duration of the mixed potential increases linearly with decreasing temperature. This result is also in agreement with the literature [14] and it enables to assume that the amount of plated lithium has also a linear trend, which suggests a possible linear trend of capacity loss.

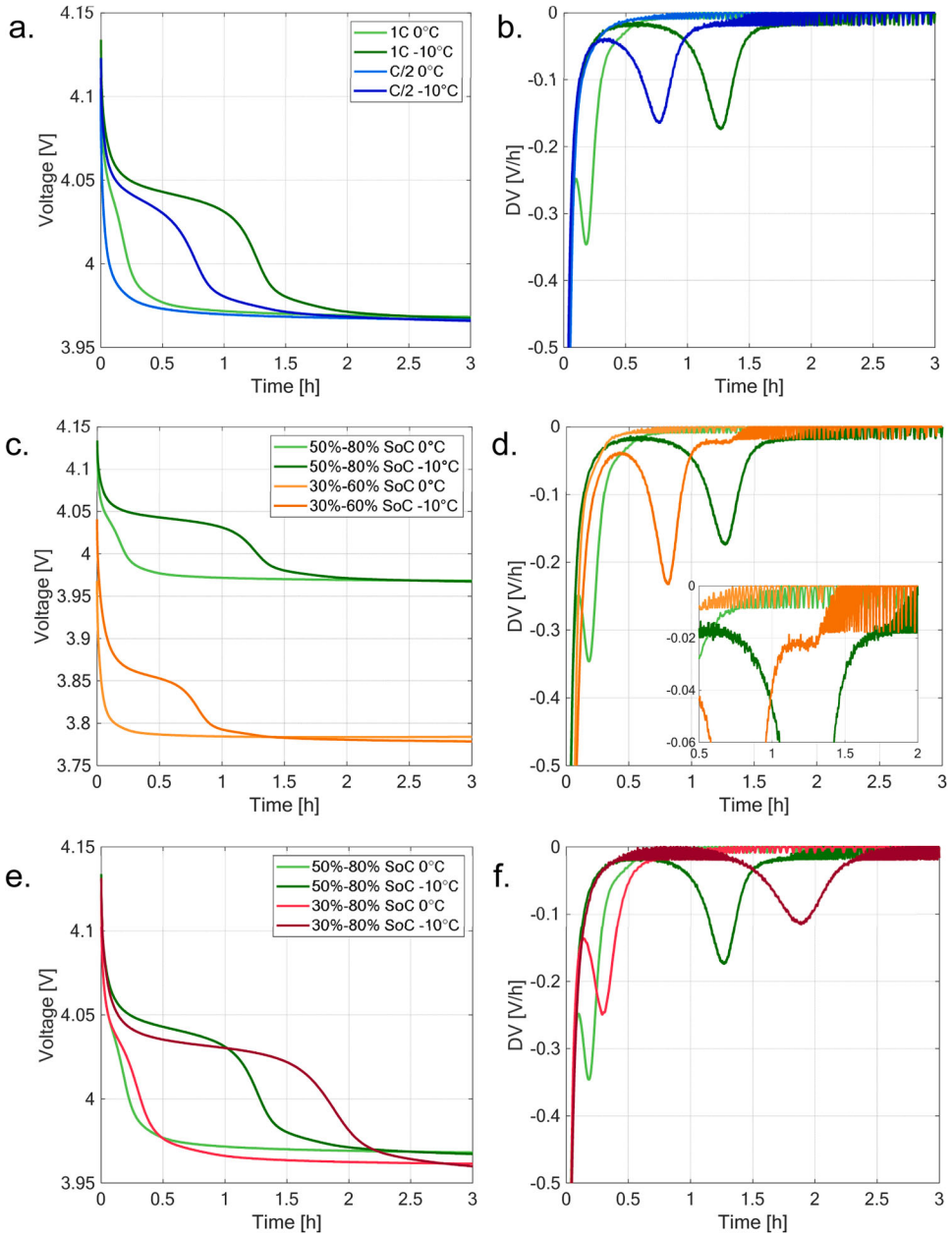

Fig. 5. Various operating conditions effects. C-rate effect: (a) measured cell voltage evolution and (b) corresponding DV for type A (50 %–80 % SoC, 1C charge, −10 °C) and B (50 %–80 % SoC, 0.5 C charge, −10 °C) pulses. *Maximum SoC effect: (c) measured cell voltage evolution and (d) corresponding DV for type A (50 %–80 % SoC, 1C charge, −10 °C) and C (30 %–60 % SoC, 1C charge, −10 °C) pulses at 0 °C and −10 °C. The inset zooms on the second peak of the 30 %–60 % −10 °C pulse. DoC effect: (e) measured cell voltage evolution and (f) corresponding DV for type A (50 %–80 % SoC, 1C charge, −10 °C) and D (30 %–80 % SoC, 1C charge, −10 °C) pulses at 0 °C and −10 °C.*

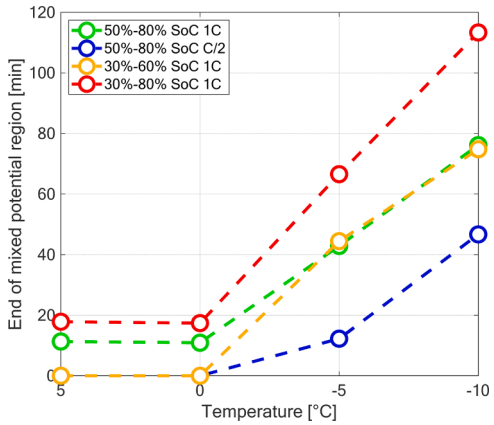

Fig. 6. Position of the peak of the DV analysis against temperature for all the pulses conditions.

Results of the cycling campaign

Capacity loss

The pulses campaign has supported the occurrence of lithium plating and provided a preliminary view of the role of the operating conditions. These observations are verified in the cycling campaign. Moreover, the performance evolution due to lithium plating at various operating conditions is investigated.

As an overview of the results, the capacity loss is exploited as indicator of degradation. The full dataset of results is available in Table 6. It is possible to notice the following trends:

- Cycles 0 vs 10: the lower the temperature, the higher the capacity loss rate. This is consistent with the results of the pulses campaign: low temperatures promote lithium plating, thus the probability of capacity loss. In the current campaign, according to the selected operating conditions, temperature is the stronger driver of degradation.
- Cycles A vs B: the higher the charging C-rate, the higher the losses. At 1C the losses are 2 to 3 times larger than at 0.5C. This trend is also in agreement with the expectations: larger currents induce larger overpotentials, thus the electrode potential decreases, approaching or overcoming 0 V. Moreover, local reaction rates increase, thus stressing the possibility of local saturation of graphite particles.
- Cycles A vs C and A vs D: the effects of the SoC window and depth of charge are more complex than the previous ones. At the beginning, high SoC induces faster losses, but proceeding with the campaign the trends differ because some evolutions slow down (e.g. except for cells A10 (50 %–80 % SoC, 1C charge, −10 °C), B10 (50 %–80 % SoC, 0.5C charge, −10 °C) and C10 (30 %–60 % SoC, 1C charge, −10 °C) that show a decreasing rate). They are discussed more in detail in subsequent analyses.

At a first sight, the role of operating conditions agrees with the results of the pulses campaign. Nevertheless, the evolution over cycles is not straightforward since most trends are almost linear, but some slow down.

One discharge was repeated to evaluate the stability of the measurement (column marked with “R” in Table 6). There is a variation of the results, larger for larger losses. It might be related to slow relaxation phenomena that were still ongoing. Lithium plating was observed to be associated with significant capacity recovery depending on the rest time after cycling [33]. As a result of this verification test, an uncertainty on the results has to be taken into account. However, the trends are confirmed, and data can be used to further investigate degradation.

In-operando analysis

In-operando variables

Fig. 7 reports the trends of voltage, C-rate and surface temperature of cell D10 (30 %–80 % SoC, 1C charge, −10 °C) at some cycle states along the campaign, both in charge and discharge in separate subfigures.

These trends are representative of the overall behaviour of this cell and, in general, of all the tested samples and operating conditions, but this cell is selected because some trends are more evident. As in the usual CCCV charge phases, the C-rate is imposed until the maximum cut-off voltage is reached (Fig. 7c) and, then, the voltage threshold is preserved (Fig. 7a), so that the charging current must decrease. At growing cycle number, the CC phase shortens. This fact is uncorrelated with the capacity loss, since all the cells are discharged to the minimum SoC referred to the nominal case, as explained in Section 2.2.2. The cell voltage hits the upper voltage limit earlier due to growing overpotentials induced by degradation. As a consequence, the CV phase extends. Only a slight difference in the temperature profile is detected (Fig. 7e). There is a surficial temperature rise by around 1.5 °C, with the peak at the beginning of the CV phase. From this point onwards, current is decreasing and so does temperature, too. When the cell ages, the temperature increase is faster and the cell experiences slightly higher temperatures despite a shorter CC phase.

On the other hand, along a discharge the C-rate is constant, without any CV phase (Fig. 7d). Temperature decreases and stabilizes around −8 °C, slightly warmer than the chamber temperature (Fig. 7f). The most interesting trend is related to the voltage: as stated in the literature, during a C/5 discharge after a low temperature charge pulse it is possible to notice the typical plateau related to the mixed potential condition of lithium stripping and deintercalation reactions, similar to what was observed in the pulses campaign. This feature occurs at every cycle, and it can be considered an indicator of lithium plating in the preceding charge. To magnify this feature, the DV of the discharge phase is performed and provided in Fig. 7g. Around 1500 s after the end of the preceding charge, there is a peak in the DV, possibly corresponding to the plateau of the mixed potential condition [29]. For this cell there is no clear trend either as magnitude or position, but this feature is then extracted as indicator of plating to compare the different cycles.

Table 6
Capacity loss for all the cycled cells at all check-ups. “R” for “repeated” attempt to evaluate the stability of the measurement.

Cell	Peculiarity	3 EFC	6 EFC	9 EFC	12 EFC	12 R EFC	15 EFC
A0	Reference case	1.9 %	2.9 %	3.6 %	4.2 %	3.5 %	4.2 %
B0	Low charge C-rate	1.1 %	1.4 %	1.8 %	2.0 %	1.6 %	2.0 %
C0	Lower SoC window	1.1 %	1.6 %	1.9 %	2.3 %	1.9 %	2.3 %
D0	Larger DoC	1.3 %	2.2 %	3.1 %	3.9 %	3.3 %	4.1 %
A10	Reference case	5.6 %	10.2 %	13.2 %	15.0 %	13.9 %	15.8 %
B10	Low charge C-rate	2.3 %	3.5 %	4.4 %	5.2 %	5.0 %	5.5 %
C10	Lower SoC window	4.7 %	10.6 %	17.1 %	22.8 %	20.4 %	24.2 %
D10	Larger DoC	3.9 %	9.1 %	14.2 %	19.8 %	17.4 %	22.8 %

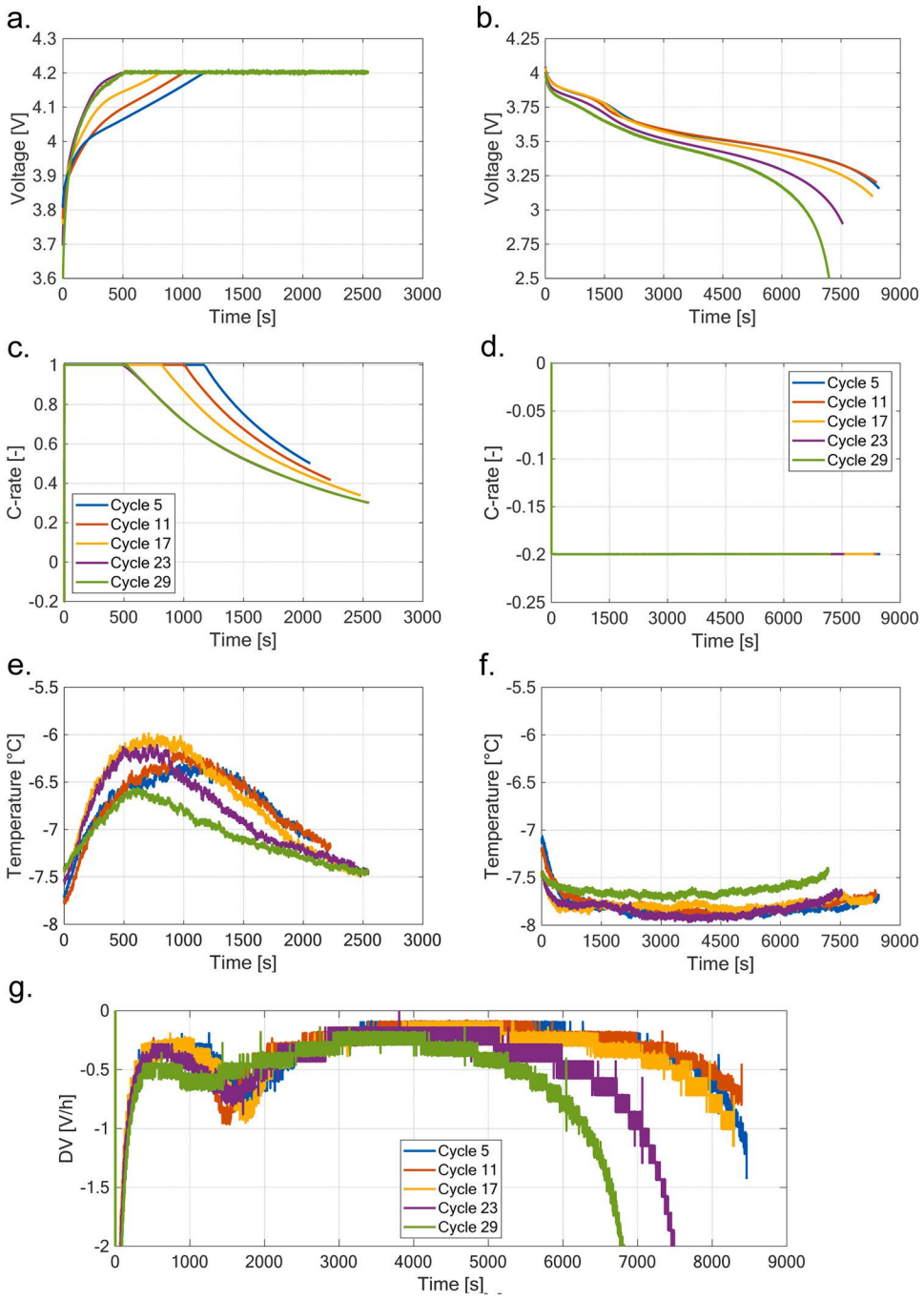

Fig. 7. Example of some charge-discharge cycles of cell D10 (charge and discharge phases are split in columns to ease the comparisons). Charge phase at different cycles: (a) cell voltage, (c) C-rate and (e) temperature profiles. Discharge phase at different cycles: (b) cell voltage, (d) C-rate, (f) temperature profiles and (g) corresponding DV analysis.

In-operando DV over discharge

Fig. 8 shows the DV of four cells, to analyse the trend at different operating conditions. The reference case A10 (50 %−80 % SoC, 1C charge, −10 °C) is provided in Fig. 8a. There is a peak around 1000 s. With respect to Fig. 7g, it seems moving towards the left and decreasing by magnitude with growing cycle number. This measurement is quite sensitive, thus it varies between close cycles, but these trends are generally shared by all the cycles on average. A decreasing trend of the position of the peak is similar to the decreasing capacity loss rate experienced by this cell.

Comparing Fig. 8a-b, the effect of the environmental temperature is highlighted (i.e. −10 °C vs 0 °C). It is very clear how signatures of lithium stripping are poorly evident at 0 °C (Fig. 8b). The first cycles have a small peak around 350 s, which becomes blurred and moves towards the left at increasing cycles, until it is no more detectable. It somehow resembles the capacity loss trend. Fig. 8c shows the trend of cell B10 (50 %−80 % SoC, C/2 charge, −10 °C). Also in this case there is a peak of decreasing identifiability, moving towards shorter time, suggesting a lower occurrence of lithium plating in the preceding charge steps, mimicking a decreasing capacity loss rate. In the last comparison, Fig. 8d shows the trend of cell C10 (30 %−60 % SoC, 1C charge, −10 °C). The stripping signature is always present, though with decreasing intensity, especially in the last cycles. Again, capacity loss and peak position seem correlated. It is therefore reasonable to associate

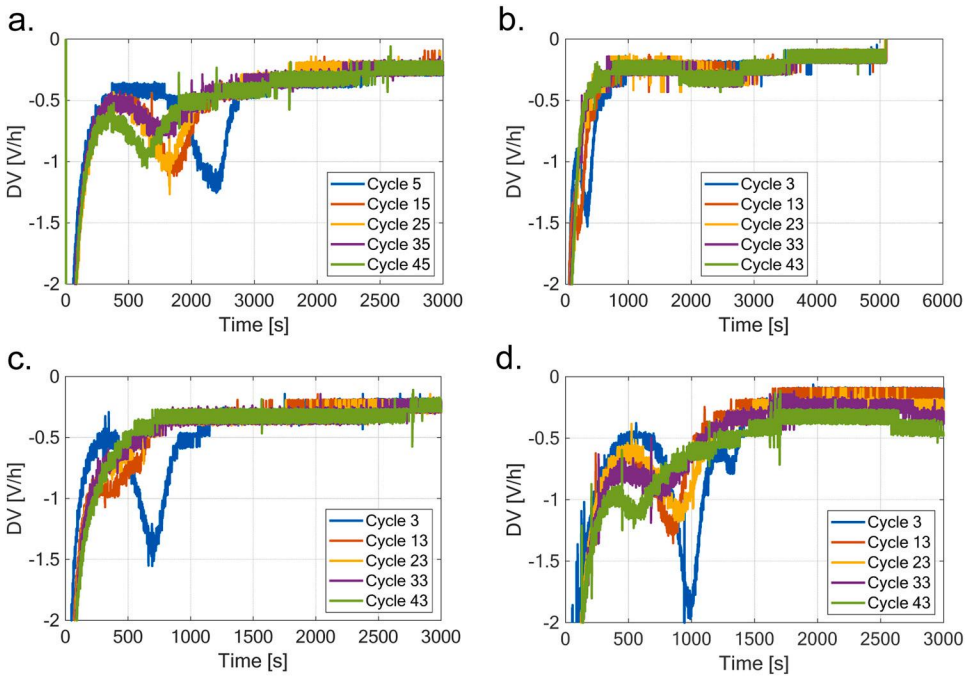

Fig. 8. DV over some discharges of cells (a) A10 (50 %−80 % SoC, 1C charge, −10 °C), (b) A0 (50 %−80 % SoC, 1C charge, 0 °C), (c) B10 (50 %−80 % SoC, 0.5C charge, −10 °C) and (d) C10 (30 %−60 % SoC, 1C charge, −10 °C) to highlight similarities and differences at varying operating conditions.

the peak position in time with the extent of the mixed potential condition and, in turn, to the amount of plated lithium.

Duration of the CV phase

The duration of the CV phase is an important variable to understand the capacity loss rate. Indeed, the longer the CV phase, the lower the average charging current at fixed charge exchange. Current affects both the overpotentials and the saturation of active sites on the surface of graphitic particles. It is clear that lower currents can be associated to a lower probability of triggering lithium plating [6,29]. This feature is more relevant for cycles:

- ending at SoC 80 %, since higher SoCs are characterized by higher OCP;
- exploiting high C-rate, because it enhances the overpotentials;
- quite high minimum SoC, because low SoC areas, characterized by high graphite OCP, are less prone to lithium plating.

From this consideration, cell A10 (50 %−80 % SoC, 1C charge, −10 °C) is expected to experience large lithium plating at the beginning, but with a decreasing trend over cycles because growing overpotentials anticipate the onset of the CV phase. Similar reasonings apply to cell B10 (50 %−80 % SoC, 0.5 C charge, −10 °C), though at a lower extent. Cycles with 30 % lowest SoC show an almost linear trend of capacity loss, since they undergo a relatively long CC phase even after tens of cycles.

Therefore, percentage of CV phase over total charging time for all cycles of the −10 °C cells (A10, B10, C10, D10) is reported in Fig. 9a, together with the capacity loss rate measured at the check-ups in Fig. 9b to identify possible similarities. The first cycle after the check-up always shows an overshoot (e.g. at every 3 EFC step), which might be related to a cold cell, with larger overpotentials. From the second cycle onwards, the duration of the CV phase has a minimum and then starts back to increase. It is easy to notice how the trends are always increasing on average. For cell A10 (50 %−80 % SoC, 1C charge, −10 °C) and B10 (50 %−80 % SoC, 0.5C charge, −10 °C), these trends flatten in the end, as the capacity loss rate, while for C10 (30 %−60 % SoC, 1C charge, −10 °C) and D10 (30 %−80 % SoC, 1C charge, −10 °C) look linear until the very last cycle batch. Moreover, at 12 EFC the campaign was interrupted for one month, before continuing with the last cycles, which explains the strong undershoot in this area. Again, from these comparisons the occurrence of lithium plating is confirmed and the role of the

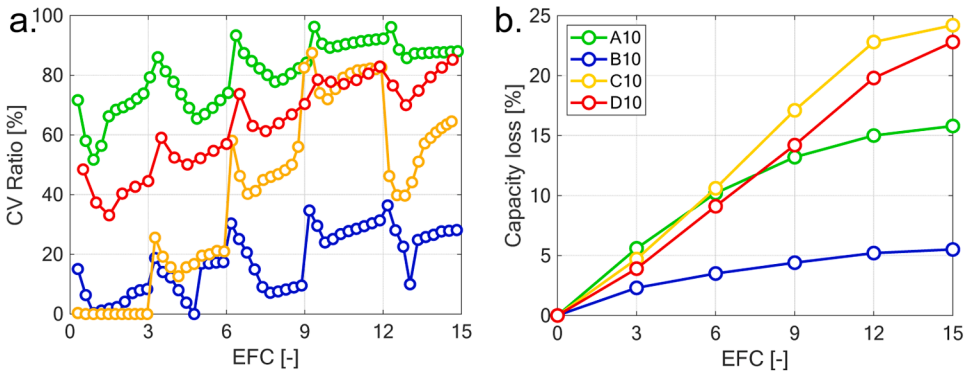

Fig. 9. (a) Duration of the CV phase for all the −10 °C cycles over cycle number. (b) Capacity loss rate over EFC.

CV phase seems definitely relevant. Moreover, due to the presence of the CV phase, lithium plating phenomenon results as self-limiting over cycling, since the limited C-rate inhibits the occurrence of the reaction. Lastly, the cycling campaign highlighted its role, which was only partially identifiable in the pulses campaign.

After the analysis of the operating conditions, the next section investigates the results of the diagnostic check-ups with the aid of the physical models, to confirm the occurrence of lithium plating and identify its signatures in the different diagnostic techniques.

Thermodynamic analysis

Experimental DV of the fresh cell

C/10 discharges at 25 °C are employed to analyse the thermodynamic losses, with the aid of the equilibrium model. First, the description of the fresh cell and the nomenclature of the main peaks and valleys is presented.

The full cell discharge curve at C/10 and 25 °C for a new cell is reported in Fig. 10c, together with single electrodes OCP curves (Fig. 10a-b) and the differential voltage curve (Fig. 10d). Electrodes OCP is measured in coin cell configuration with lithium counter electrode. Fig. 10a shows two flat regions around 4.1 V and 3.9 V which are typical of LMO, while the large plateau at 3.7 V is associated to NMC [34,35]. In Fig. 10b, the graphite OCP shows three distinctive plateaus. As known in the literature [36], the largest one between 50 % and 100 % lithiation level refer to the phase transition between LiC12 and LiC6 and it is associated to a potential of 80 mV Li/Li+ . The second stage, between 25 % and 50 %, is associated to the coexistence of LiC18 to LiC12 phases and shows a potential of 120 mV. In the last part, three plateaus may be present, but for this graphitic material only one clear flattening is observed.

The comparison between full cell and single electrodes curves is here exploited to understand the operation of the sample. The green curve in Fig. 10c and Fig. 10d is the best matching of electrodes OCP to reproduce

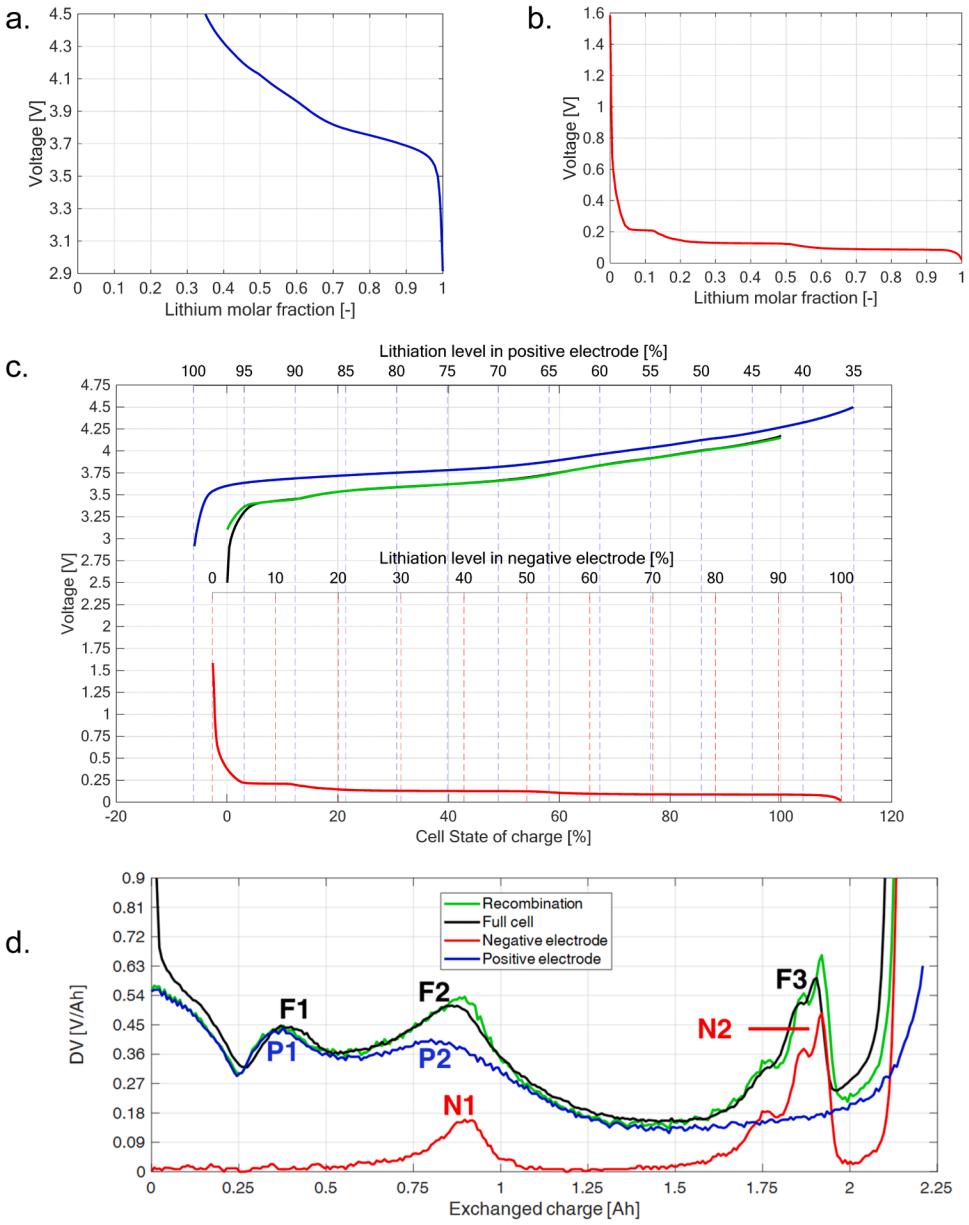

Fig. 10. OCP relation with lithium molar fraction of (a) positive and (b) negative electrodes. (c) Discharge curve and (d) corresponding DV of a fresh cell, with electrodes OCP. Black curve for experimental curve, while the green one is best matching of electrodes OCP. Red and blue for negative and positive electrodes OCP, respectively.

the experimental full cell curve (black). From left to right of the DV chart, there are two peaks F1 and F2 of the full cell, attributed to the phase transitions of LMO (P1 and P2). After that, there is a peak N1 (red curve) corresponding to the moving from the first to the second plateau of graphite on the negative electrode, which is superimposed to P2, resulting in the F2 feature.

Here there is a wide valley, where both electrodes pass through a large phase transition. At low SoC, graphite follows three short phase transitions (N2), that end with a steep voltage increase, corresponding to the almost fully delithiated state, which makes the cell voltage drop down to the minimum voltage. The OCP of positive electrode starts to fall steeply because the electrode is almost fully lithiated, but this is not the limiting electrode at begin of life state.

Experimental DV of aged cells

Experimental trends of aged cells are showed. Fig. 11a shows different differential voltages of cell A10 (50 %−80 % SoC, 1C charge, −10 °C). Lines facilitate the reading. In this qualitative view, the area until 0.5Ah looks almost unchanged.

For instance, the first valley at 0.25Ah does not move away with respect to the blue line, which is a proxy of limited LAMp. The peak F2 position, originally at 0.9Ah, is traced by the red line. It moves to the left, with a rate that can be approximated with two lines of different slopes, indicating a slowdown of this phenomenon. Similarly, the second red line follows the peak F3, associated with N2 of graphite at low SoC, which is approximated through two differently sloped lines. It is worth mentioning that the slope of the red lines is different, thus there exist different phenomena for these trends. Fig. 11b shows a selection of curves in the usual plot, to ease the comparison of the main features. From left to right, F1, related to P1 of the positive electrode, is almost unchanged, except for a slight increase in magnitude for very aged states. The trend of the F2 is very interesting: it always moves to the left, but the magnitude has a maximum around 3 EFC. After that, the valley lifts up while the peak decreases. Lastly, F3 significantly moves to the left, while becoming less defined.

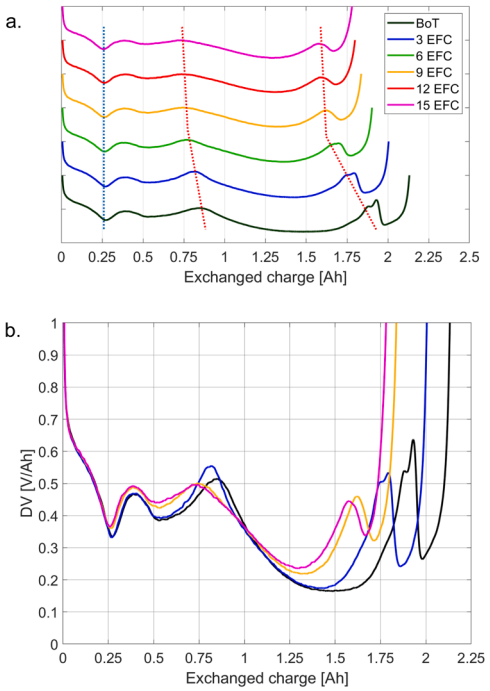

Fig. 11. (a) Differential voltage of cell A10 (50 %−80 % SoC, 1C charge, −10 °C) at different degradation states. Lines ease the detection of peaks/valleys movement. (b) Differential voltage of some degradation states to compare the peaks/valleys magnitude.

Modelled DV

Fig. 12 shows the solution of the model for cell A10 (50 %−80 % SoC, 1C charge, −10 °C) against the experiments. From Fig. 12a, the general trends are well captured, except for the very first tail which is related to the transient at beginning of discharge, which is not implemented in the equilibrium model. At low SoC, peak F3 is progressively blurred and the following valley is shortened and lifts up in the experiments, while the model simulates it as at exact equilibrium. This feature is more evident in Fig. 12b. As discussed in Section S2.3 of the Supplementary Materials, this difference might be related to a C-rate effect, which is not included in the model: as the cell ages, C/10 might not be low enough to avoid significant heterogeneity in the electrode behaviour, resulting in a more dispersed and blurred signature. It means that the assumption of close-to-equilibrium is not fully satisfied on very aged cells. The same reasoning applies at high SoC, where F2 is blurred and the valley is increasing. Similar observations were performed on coin cells of harvested materials aged in different conditions with respect to this campaign, but they are likely to be extended to the present case.

The model shifts the graphite OCP to the left and simulates degradation through the superposition of one LMO and one graphite peak (Fig. 12c), namely P2 and N1. At fresh state or begin of life (BoL), the peaks are not matched, but little lithium loss makes N1 moving to the left, summing up to the LMO peak. This fact explains the growing magnitude of the peak at 3 EFC in the experiments. From this point onwards, the peaks decouple again due to a growing lithium loss, so that graphite peak N1 overlaps with the valley. The model shows the graphite peak between the positive electrode ones clearly (Fig. 12b, 15 EFC), while it is reflected only in a valley increase in the experiments. Again, this blurred signature can be associated with a relatively high C-rate, which does not fully respect the close-to-equilibrium assumption. Lastly, the slight increase of the first peak is likely to be associated to the same phenomenon: the graphite peak is dispersed and it is partially present already at 0.35Ah, overlapping with the LMO peak.

Thermodynamic parameters evolution

Model simulations are satisfactorily in agreement with the experiments. In Fig. 13, the trends of physical parameters are reported for cell A10 (50 %−80 % SoC, 1C charge, −10 °C), with a confidence band, as explained in Section 2.5. A brief critical analysis is here presented.

LLI (green curve in Fig. 13) is the dominant mechanism, with an evolution that resembles that of the capacity loss. Its value is relatively defined (little width of the confidence band), since its variation affects the residual capacity in a sensible way. According to the sensitivity analysis reported in Section S1 of the Supplementary Materials, it is responsible for the shift of the graphite OCP curve, thus it induces the coupling-decoupling of peaks between LMO and graphite at high SoC and the leften movement of the F3 peak. LLI is a direct consequence of lithium plating [5,7].

On the other hand, both LAM values are relatively low and quite spread (wide confidence band at high EFC values). The progressive increase in confidence bands along ageing is the consequence of different aspects. First, the complexity of the models in fully reproducing the behaviour of aged cells. Second, the C-rate effect on C/10 discharge curve, as already discussed. Lastly, the limited identifiability of some parameters which affect the model solution at a limited extent.

For the present case, according to the sensitivity analysis, for low LAMp extents the most interesting feature occurs at high SoC, where positive electrode peaks move to the left, slightly closing one to each other and their magnitude increases. This last characteristic is similar to that of the experiments, suggesting the algorithm to raise LAMp value. However, this effect is only a little significant on numerical basis, but it is not enough to clearly assess a growth of this parameter, which, indeed, has a large uncertainty. Considering the C-rate effect already discussed, which can affect the positive electrode peaks, and considering that this effect is not implemented in the equilibrium model, it is likely that the algorithm is mistaking the C-rate effect as a degradation effect. Thus, it is

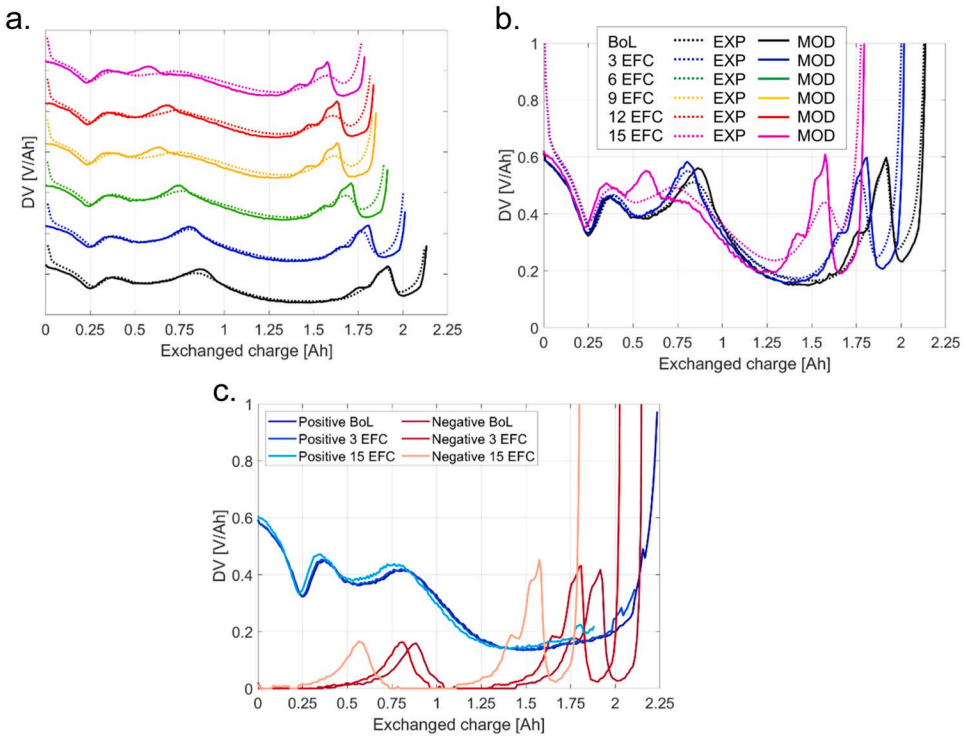

Fig. 12. Experimental (dashed lines) and model (full lines) differential voltage curves of cell A10 (50 %−80 % SoC, 1C charge, −10 °C). (a) Qualitative trend of all ageing states. (b) Selection of check-ups for quantitative analysis. (c) Variations of the electrodes OCP matching.

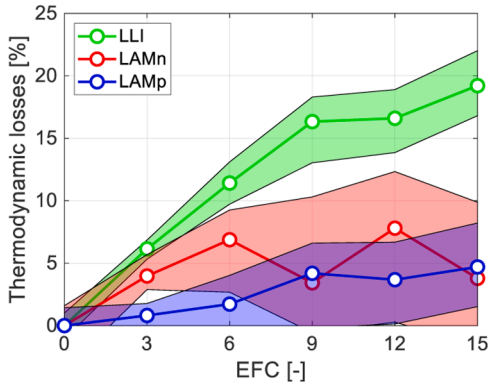

Fig. 13. Trend of thermodynamic parameters of cell A10 (50 %−80 % SoC, 1C charge, −10 °C): LLI (green), LAMp (blue) and LAMn (red). Full lines with markers for optimal values, semi-transparent areas for confidence bands.

assumed that there is no strong evidence of LAMp and thus it is assumed to be null, as already pointed out in the analysis of Fig. 11a.

On the other hand, LAMn at low extents affects the utilization of the first and second graphite stages, thus shifting the graphite peak N1 position at high SoC. Due to the C-rate effect, the peak induces a significant error on the cost function, that the algorithm aims at minimizing. A little LAMn slightly improves the cost function, but its value can't be determined clearly. As in Fig. 11a, the different sloped of red lines suggest that a little LAMn is likely to be present, but it is a second-order effect with respect to LLI.

Data for all the 8 cells are reported in Table 7. Confidence bands are avoided to improve readability. The dominance of LLI at −10 °C is confirmed, though at different rates depending on the operating conditions, as observed for the capacity loss trend. However, some relevant unexpected trends exist, namely the large LAMn of 0 °C cells and the negative LAMn of cells C10 (30 %−60 % SoC, 1C charge, −10 °C) e and D10 (30 %−80 % SoC, 1C charge, −10 °C). These results require a deep analysis, reported in Section S3 of the Supplementary Materials. From this activity it is clear how it is possible to assume that almost all the cells exhibit a LAMn in the order of 6 %−10 %, which stabilizes, and discrepancies can be regarded to a C-rate effect.

Table 7
Results of the thermodynamic analysis for all the tested cells at all the check-ups.

Parameter		Ageing state					
		BOL	3 EFC	6 EFC	9 EFC	12 EFC	15 EFC
A10	LLI	0.0%	6.1%	11.4%	16.3%	16.6%	19.2%
	LAMp	0.0%	0.8%	1.7%	4.2%	3.7%	4.7%
	LAMn	0.0%	4.0%	6.9%	3.4%	7.8%	3.8%
B10	LLI	0.0%	2.3%	4.0%	5.1%	6.5%	6.9%
	LAMp	0.0%	0.3%	1.1%	1.1%	1.8%	2.1%
	LAMn	0.0%	5.1%	6.7%	7.1%	7.8%	8.8%
C10	LLI	0.0%	4.9%	11.9%	20.3%	28.7%	30.4%
	LAMp	0.0%	0.5%	2.1%	4.5%	7.5%	7.8%
	LAMn	0.0%	4.6%	6.8%	2.7%	-7.1%	-7.1%
D10	LLI	0.0%	4.6%	10.9%	17.8%	24.0%	28.1%
	LAMp	0.0%	0.8%	2.3%	4.7%	5.4%	6.9%
	LAMn	0.0%	4.9%	6.9%	2.9%	2.7%	-7.0%
A0	LLI	0.0%	2.5%	3.9%	5.3%	6.5%	7.4%
	LAMp	0.0%	0.6%	0.9%	1.3%	1.8%	2.8%
	LAMn	0.0%	4.9%	5.6%	6.6%	7.5%	8.7%
B0	LLI	0.0%	1.6%	1.9%	2.5%	2.7%	3.2%
	LAMp	0.0%	0.8%	0.7%	1.0%	0.9%	1.6%
	LAMn	0.0%	9.3%	9.4%	10.0%	10.8%	11.8%
C0	LLI	0.0%	1.8%	2.7%	3.2%	3.4%	3.7%
	LAMp	0.0%	0.6%	1.2%	1.3%	1.3%	1.7%
	LAMn	0.0%	5.1%	6.3%	6.6%	7.2%	7.6%
D0	LLI	0.0%	2.4%	3.7%	4.8%	5.8%	6.2%
	LAMp	0.0%	1.1%	1.6%	1.8%	2.0%	2.4%
	LAMn	0.0%	4.7%	5.6%	6.7%	7.7%	7.6%

Kinetics and mass transport

Experimental trends

The behaviour far from equilibrium is now investigated, exploiting the procedure described in Section 2.5. First, the experimental trends are summarized, then the trends of the physical parameters are presented and discussed. As for the thermodynamic part, cycle A10 (50 %−80 % SoC, 1C charge, −10 °C) is selected to provide an example of results. Fig. 14 shows its behaviour of cell A10 in all tests and all the check-ups. Fig. 14 a-b present the evolution of EIS. The shape of the spectrum is not affected by degradation at a large extent, still showing one semicircle followed by a low frequency tail. The HFR increases slightly, while the kinetic loop increases progressively with cycling. The peak of the semicircle shifts to lower frequency, too, indicating the worsening of at least one reaction, while there is no substantial difference for frequencies higher than 50 Hz. The low frequency part is poorly affected only at the last stages, where the loop partially overlaps due to the frequency shift. Fig. 14 c-d provide similar information, though at higher temperature the magnitude of the variations is limited. Lastly, Fig. 14 e-f show the behaviour during discharge. The capacity reduction is very clear from Fig. 14 f, even though it is lower than what is measured during a full C/10 discharge. In both cases, a clear polarization growth is evident, as already highlighted in the analysis of the EIS, possibly related to a worsening of the kinetics. A model is required to derive further considerations.

A comparison (one discharge and one EIS) for all the −10 °C cycled samples (A10, B10, C10, D10) are reported in Section S4.1 of the Supplementary Materials, to visualize that trends are similar, but showing a large spread, which reflects the different degradation extent experienced by the cells. Cycle C and D (charging between 30 %−60 % SoC and 30–80 % SoC respectively) exhibit the largest changes with respect to the BoL state. Cycle A and B (charging at 1C and 0.5C respectively), in turn, looks like intermediate states of the same trends.

Modelling results

The identification of physical parameters is performed for the three most aged cells only, namely A10 (50 %−80 % SoC, 1C charge, −10 °C), C10 (30 %−60 % SoC, 1C charge, −10 °C), and D10 (30 %−80 % SoC, 1C charge, −10 °C), to understand the strongest trends and possible variability among cells. Two ageing states, 9 EFC and 15 EFC, are considered.

First, a direct comparison of experiments and model simulations is provided in Fig. 15. The model simulates the growth of the kinetic arc, together with the frequency shift (Fig. 15a-b). It overestimates the enlargement at ambient temperature (Fig. 15c-d), trading-off with the slight underestimation at 10 °C. This feature suggests that the temperature dependence can be improved, but this is out of scope for this work. Regarding the discharge, the model reproduces the 25 °C 1C (Fig. 15f) properly, showing a good fit of the polarization losses. The variation of the extractable capacity is strong, even though it is not perfect. On the contrary, the 10 °C 2 C discharge is much more challenging. The model simulates a long transient, more evident than in the experiments, due to a limited lithium transport in graphite particles. However, larger solid-state diffusivities would further overestimate the extractable capacity in the 25 °C partial discharge. Overall, this compromise is satisfactorily.

Trend of kinetic and mass-transport parameters

The trend of physical parameters for cell A10 (50 %−80 % SoC, 1C charge, −10 °C) is depicted in Fig. 16. The most important trend is related to the electrolyte conductivity (Fig. 16a). For the most aged cells,

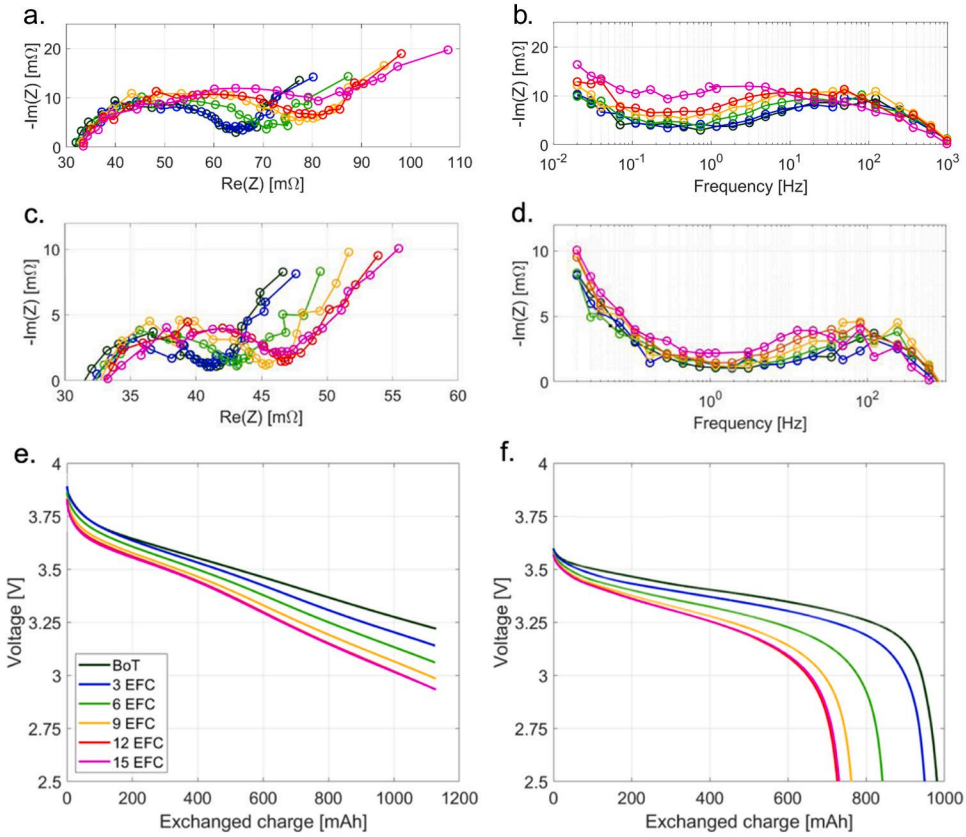

Fig. 14. Experimental measurements belonging to the check-up procedure, performed every 3 EFC on cell A10 (50 %−80 % SoC, 1C charge, −10 °C): (a-b) Nyquist and Bode plot of the imaginary component of the impedance, recorded at 100 % SoC and 10 °C; (c-d) Nyquist and Bode plot of the imaginary component of the impedance, recorded at 50 % SoC and 25 °C; (e) discharge at 10 °C 2 C, from 100 % to 50 % SoC; (f) discharge at 25 °C 1C, from 50 % SoC to the minimum voltage level.

a decrease by 50 % of the electrolyte conductivity is estimated. It is worth remembering that electrolyte conductivity and diffusivity are related through the Nernst-Einstein relation [37], thus if one varies the other does, too, by the same multiplication factor. Hence, electrolyte properties are the main contributors to the polarization increase that was observed in the discharge of aged cells. Moreover, they cover the slight increase of HFR in EIS and portion of the kinetic loop. This parameter might either be associated to the electrolyte properties itself or to the SEI that has grown consuming plated lithium and electrolyte material, resulting in an additional barrier to ion transport [5–7].

Nevertheless, this parameter is not enough to fully reproduce the experimental data. The evolution of the impedance spectrum suggests that at least one reaction is worsening. According to some observations on the same cell type, but aged in different conditions, it is assumed that the double layer capacitance of the negative electrode should remain constant. This choice is required to let the algorithm discriminate between the charge transfer resistance of the two electrodes and achieve a stable result. According to this assumption, an increase of the capacitance of the double layer of the other electrode is obtained (Fig. 16b), which follows the frequency shift already observed in the experiments. Even though a marked difference exists in experimental EIS, the trend of the kinetic rate constants is doubtful (Fig. 16c-d). No further considerations can be drawn, since their trend is not stable. Worsening of charge-transfer of both electrodes or the contribution of the SEI might be the cause.

Lithium solid-state diffusivity into positive electrode (Fig. 16e) does not show a clear trend and its value has a wide uncertainty. When this parameter can assume larger value than at BoL condition it means that diffusion in this electrode is not a limiting phenomenon, thus its effect is not detectable from the discharge. Therefore, no effect is associated to this parameter, which is assumed to be almost constant. This is in agreement with the expectations.

On the contrary, lithium solid-state diffusivity in graphite (Fig. 16f) has an unexpected role. Indeed, degradation is supposed to induce a worsening of transport phenomena. In this case, the parameter seems growing with ageing, though with large uncertainty. The reason for this result is found in the following feature. As already mentioned regarding Fig. 14 f, the extractable capacity at 1C decreases over cycling, but this reduction is lower than the measured capacity loss at close-to-equilibrium conditions. This fact suggests an improved performance at high C-rate, which may be the result of increased self-heating due to larger irreversibilities. However, no major difference is recorded in the temperature profile along the discharge. Moreover, thermal properties are kept constant in this parameter identification procedure. As a result, graphite diffusivity must increase to account for this effect. Nevertheless, this parameter might also reveal an ongoing mechanism. For simplicity, the difference between C/10 and 1C capacities is labelled ΔCap. Indeed, the ΔCap of cell A10 (50 %–80 % SoC, 1C charge, −10 °C) is reported in Fig. 17a. Its variation is sudden at the beginning, then almost stabilizes. This trend is very similar to that of LAMn. Due to the above-mentioned limitations in the estimation of LAMn, the one of cell B10 (50 %–80 % SoC, 0.5C charge, −10 °C) is reported for comparison in Fig. 17b. One possibility is that LAMn refers to a mechanism like particle cracking, which, on one side, makes a portion of the electrode inactive, thus inducing LAMn, but on the other side it forms smaller particles. Small particles have a faster diffusion, because the path for solid diffusion of lithium is reduced. Therefore, this parameter might mimic an improved diffusion which is not related to the property

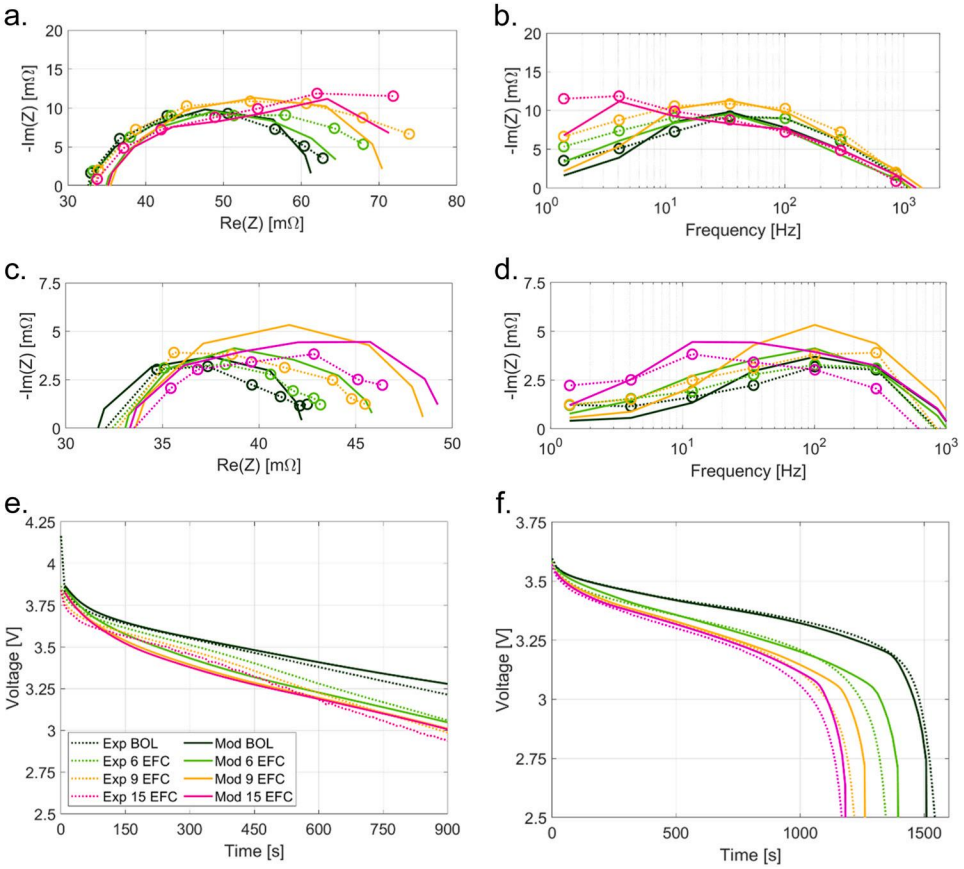

Fig. 15. Model simulations (full lines) and experimental curves (dashed) of the tests belonging to the check-up procedure for selected ageing states of cell A10 (50 %–80 % SoC, 1C charge, −10 °C): (a-b) Nyquist and Bode plot of the imaginary component of the impedance, recorded at 100 % SoC and 10 °C; (c-d) Nyquist and Bode plot of the imaginary component of the impedance, recorded at 50 % SoC and 25 °C; (e) discharge at 10 °C 2 C, from 100 % to 50 % SoC; (f) discharge at 25 °C 1C, from 50 % SoC to the minimum voltage level.

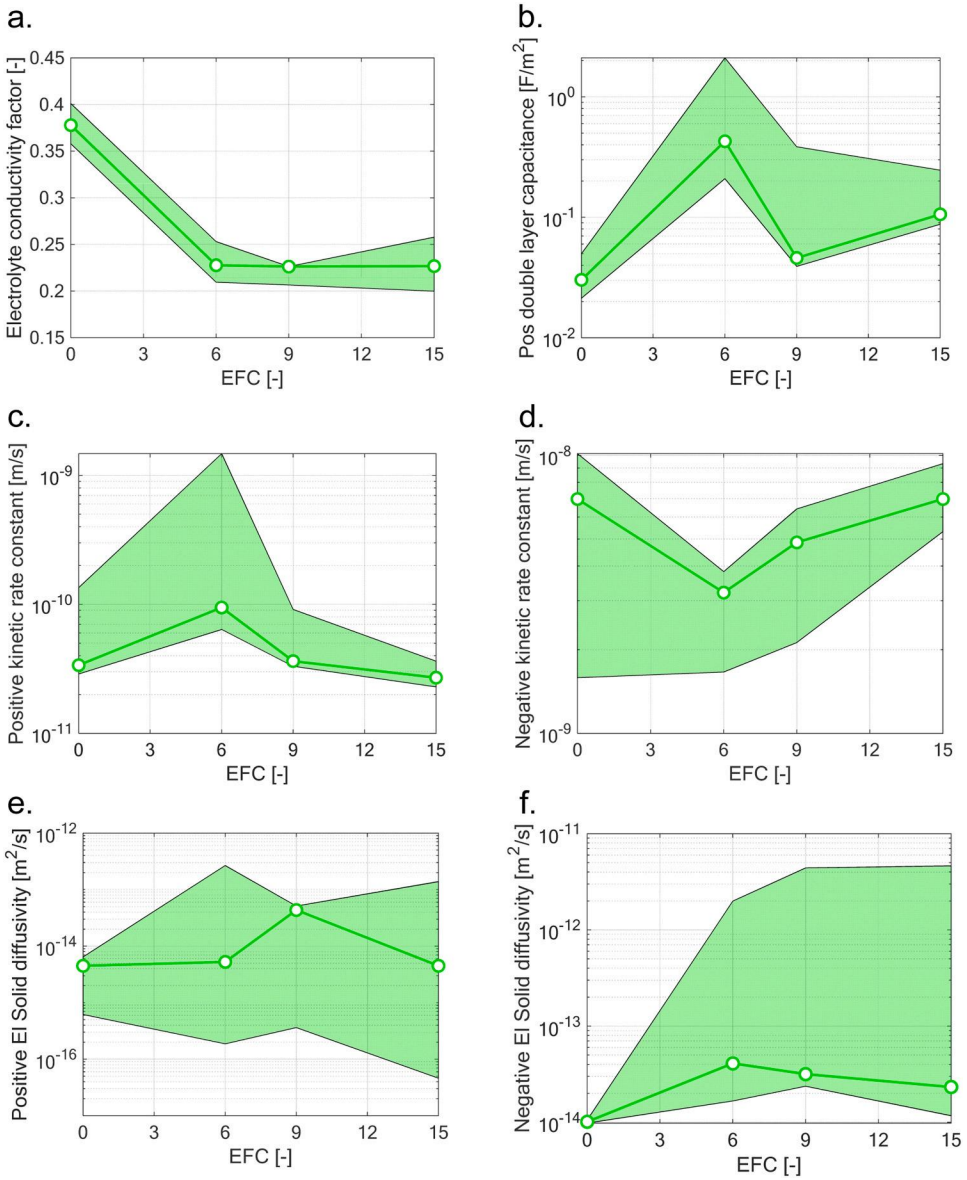

Fig. 16. Trend of physical parameters of cell A10 (50 %−80 % SoC, 1C charge, −10 °C) over EFC with confidence bands: (a) electrolyte conductivity factor; (b) double layer capacitance of the positive electrode; kinetic rate constant of (c) positive and d) negative electrodes; solid-state diffusivity of lithium into e) positive and f) negative electrode particles.

itself, but to the different particle size.

Lastly, parameters evolution of cells C10 (30 %−60 % SoC, 1C charge, −10 °C) and D10 (30 %−80 % SoC, 1C charge, −10 °C) are showed in Section S4.2 of the Supplementary Materials for the sake of completeness. They are comparable with A10 (50 %−80 % SoC, 1C charge, −10 °C), as expected from the experiments.

Simulation of discharge of an aged cell

The use of a physical model has the advantage of showing the evolution of variables like concentrations which are not available experimentally, to understand the behaviour of the cell. One clear example is here reported for the 2 C 10 °C discharge, which has the largest variation with ageing. The voltage profile is reported in Fig. 18a, while the local current generation in Fig. 18b for some time instants along the discharge, for both the electrodes thickness. The operation is strongly heterogeneous. At the beginning, a large utilization is associated with the area close to the separator or both electrodes, because the low electrolyte conductivity favours a short path for ion movement. With increasing time, the distribution of current becomes more uneven, due to local variation of the overpotential and the equilibrium potential. Nevertheless, the region close to the separator still shows the largest utilization, as confirmed by the concentration profiles in Fig. 18c. After 10 min from the beginning of discharge, graphite is almost delithiated at the interface with the separator, while no great difference occurs at the current collector due to a too long path for ion movement. From this instant onwards, Li ions are forced to reach the middle of the electrode thickness, where the peak of the current source is evident, because graphite OCP is too large close to the separator. As a result, the peak of the current source progressively shifts towards the current collector and the lithium content behaves correspondingly. This trend is similar on the positive electrode side, though at a lower extent. Lastly, dashed lines in Fig. 18c refer to the concentration inside the spherical particles. In the positive electrode, dashed and full lines are hardly distinguishable, according to a quite low characteristic time for diffusion thanks to the relatively small particle radius. On the contrary, the concentration gradient in graphitic particles is easily identifiable, due to the large particles. This gradient further exacerbates the transport limitations.

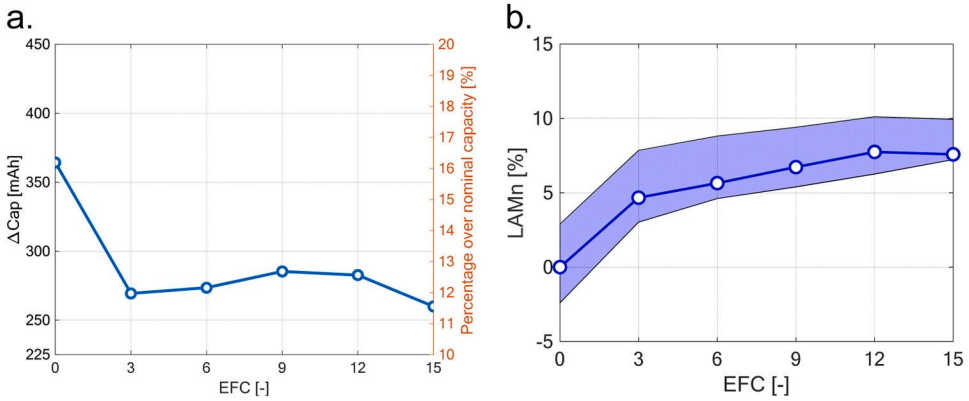

Fig. 17. (a) Trend over EFC of ΔCap of cell A10 (50 %−80 % SoC, 1C charge, −10 °C) and of (b) LAMn of cell B10 (50 %−80 % SoC, 0.5C charge, −10 °C).

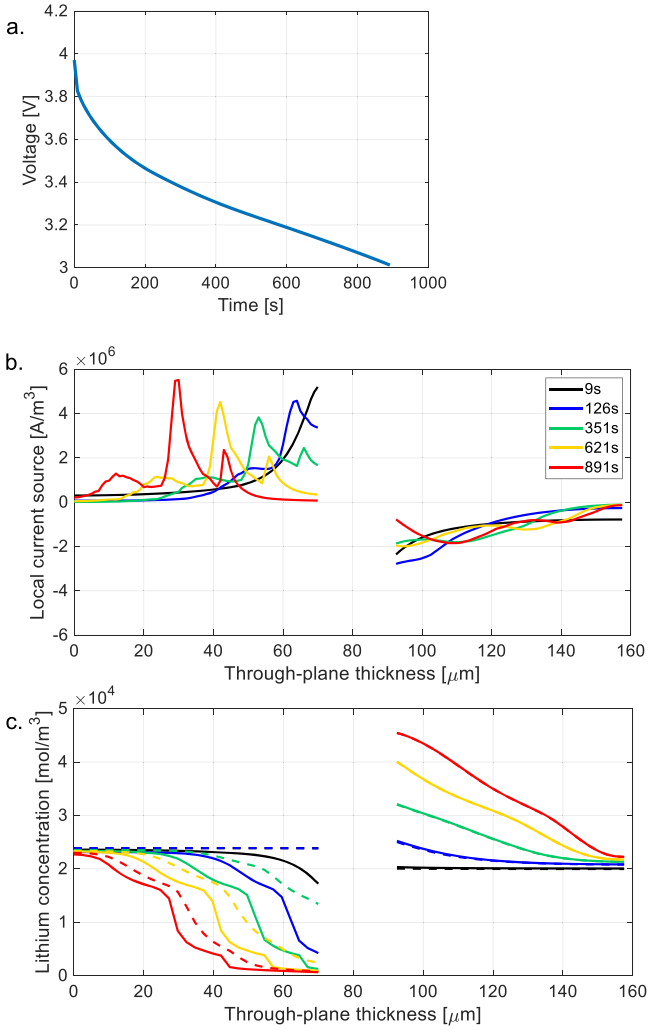

Fig. 18. Model simulation of 10 °C, 2C discharge from 100 % to 50 % SoC for cell A10 (50 %−80 % SoC, 1C charge, −10 °C) after 15 EFC. (a) Voltage profile, (b) Volumetric current sources over electrode thickness at specific time instants. (c) Lithium concentration on surface (full lines) and centre (dashed) of electrode particles at specific time instants.

Interpretation of the results

As a final summary, the main remarks are here reported. The cycling campaign provides consistent results with the early observations during pulses. Capacity loss is almost linear with EFC and the operating conditions provide analogous effects to the pulses case: low temperature, high charging C-rate and high DoC and SoC promote the occurrence of lithium plating. However, the time-evolution of high-SoC cycles has a decaying trend, because the imposed maximum voltage threshold forces a large CV phase, in which decreasing C-rates becomes less detrimental for the device. Moreover, the DV analysis of the C/5 discharge during cycles appeared to provide similar insights to the relaxation after pulses, supporting the decreasing lithium plating of high SoC cycles.

The thermodynamic analyses revealed a significant lithium inventory loss, similar to the capacity loss trend and with similar dependence on the operating conditions of the cycles. On the contrary, the identification of LAM posed some questions due to the raise of important heterogeneity of operations, which affected the close-to-equilibrium assumption. With a critical analysis of experimental and modelling curves, the absence of degradation to the positive electrode is confirmed, while a limited extent of active graphite loss takes place, which was deeply investigated. LAMn increases very fast, disregarding the operating conditions, and stabilizes at 6 %−10 %, due to an intrinsic stabilization process of the material.

Aged cells showed evolution of the impedance spectrum, especially at low temperature, suggesting a worsening of the kinetics, while overpotentials increase during discharge. The model was able to reproduce the main trends and the most important parameter is the conductivity of the electrolyte. This parameter is attributed to the decomposition of the electrolyte, due to side reaction with plated lithium to form SEI. Both LLI and electrolyte conductivity evolution are consistent with the occurrence of lithium plating [5–7].

The unexpected growth of the solid-state diffusivity of lithium in graphite was related to particle cracking, according to the similarity with LAMn trend and to the difference between extractable capacity at C/10 and 1C. Regarding EIS, the evolution of the charge transfer area is too little to provide a reliable interpretation, since the variation of the parameters is within the confidence band. Worsening of charge-transfer of both electrodes or the presence of the SEI are possible explanations. Lastly, no difference is observed between the tested cells except for the different LLI extent.

Conclusions

The behaviour of the samples at low temperature was investigated as case study for the application of an optimized procedure for diagnosis. First, a pulses campaign was conducted to understand the role of the operating conditions exploiting the evolution of voltage over relaxation after a pulse and to verify the occurrence of lithium plating. The results support the occurrence of lithium plating and the magnitude of the plateau increases with low temperature, high C-rates, high SoC and high DoC. The possibility of a double-stage plateau is addressed by analysing

the pulse between 30 % and 60 % SoC, which might be related to the transition from first to second stage of graphite during the relaxation. Lastly, the extension of the mixed potential condition seems to increase linearly at decreasing temperature below 0 °C, which is a valuable information to predict capacity loss. This campaign is the starting point of the cycling campaign, which allowed to understand the effect of sequences of plating events.

The main outcomes are here reported.

- Capacity loss decreases very fast in the tested conditions (up to 1.5 %/EFC), especially for low temperature and high charging rate cases.
- Cycles at high SoC shows an extended CV phase during charge, which self-limits the occurrence of lithium plating.
- Peaks in the DV analysis of discharge show similarities with the pulses campaign. Moreover, their position in time seems correlated with the capacity loss rate.
- DVA at q-OCP highlights a dominant role of LLI, consistent with lithium plating.
- Large electrolyte consumption is detected, possibly related to the reaction between plated lithium and the electrolyte, forming SEI. This is the strongest evidence, inducing a strongly anisotropic utilization of the electrodes during discharge, as simulated by the model.
- Other than these features, no peculiar trend due to lithium plating is observed in the remaining parameters evolution.

Overall, this work provides reasonable results with respect to the existing literature, integrating it with an in-depth analysis of degradation at low temperature and its promoting conditions. Overall, it demonstrates the feasibility of an holistic diagnostic and interpretation methodology, relying on physical-based investigation, previously lacking within the scientifical literature where the focus was typically put on a single aspect at a time. Under the methodology perspective, the combined use of experiments and models provided useful insights, supporting the identification of the degradation mechanism and enabling to understand the effect on the operation of the battery. Considering that the results obtained are well consistent with the selected plating-dominated case-study, we can assume valid the proposed methodology in providing an innovative physical-based interpretation of battery ageing. This case study paves the way to the application on more realistic conditions, which is topic of the forthcoming publications.

CRediT authorship contribution statement

Gabriele Sordi: Conceptualization, Methodology, Investigation, Formal analysis, Data curation, Validation, Visualization, Writing – original draft, Writing – review & editing. **Melissa Sedzik:** Conceptualization, Investigation, Formal analysis, Visualization. **Andrea Casalegno:** Supervision, Writing – review & editing, Project administration, Funding acquisition. **Claudio Rabissi:** Conceptualization, Supervision, Writing – review & editing, Project administration, Funding acquisition.

Declaration of Competing Interest

The authors declare that they have no known competing financial interests or personal relationships that could have appeared to influence the work reported in this paper.

Data availability

Matlab code of the model is made available at https://doi.org/10.5281/zenodo.13905429.

Acknowledgements

This work was supported by the European Union's Horizon 2020 Research and Innovation Program [Grant Agreement No. 873111, project "DigiPrime - Digital Platform for Circular Economy in Cross-sectorial Sustainable Value Networks"] and the Energy for Motion initiative of Politecnico di Milano as part of Energy department recognition as Department of Excellence 2018–2020 from Italian Ministry of Education, Universities and Research (MIUR).

Appendix A. Supporting information

Supplementary data associated with this article can be found in the online version at doi:10.1016/j.fub.2024.100006.

References

[1] Z. Wang, X. Zhao, L. Fu, D. Zhen, F. Gu, A.D. Ball, Sustain. Energy Technol. Assess. 60 (2023), https://doi.org/10.1016/j.seta.2023.103457.
[2] G. Sordi, C. Rabissi, A. Casalegno, Energ. (Basel) 16 (2023), https://doi.org/10.3390/en16124730.
[3] C. Rabissi, A. Innocenti, G. Sordi, A. Casalegno, Energy Technol. 9 (2021), https://doi.org/10.1002/ente.202000986.
[4] C. Rabissi, G. Sordi, A. Innocenti, A. Casalegno, J. Energy Storage 59 (2023), https://doi.org/10.1016/j.est.2022.106435.
[5] M. Petzl, M. Kasper, M.A. Danzer, J. Power Sources 275 (2015) 799–807, https://doi.org/10.1016/j.jpowsour.2014.11.065.
[6] M. Ecker, P. Shafiei Sabet, D.U. Sauer, Appl. Energy 206 (2017) 934–946, https://doi.org/10.1016/j.apenergy.2017.08.034.
[7] J.S. Edge, S. O'Kane, R. Prosser, N.D. Kirkaldy, A.N. Patel, A. Hales, A. Ghosh, W. Ai, J. Chen, J. Yang, S. Li, M.C. Pang, L. Bravo Diaz, A. Tomaszewska, M. W. Marzook, K.N. Radhakrishnan, H. Wang, Y. Patel, B. Wu, G.J. Offer, Phys. Chem. Chem. Phys. 23 (2021) 8200–8221, https://doi.org/10.1039/d1cp00359c.
[8] C. Uhlmann, J. Illig, M. Ender, R. Schuster, E. Ivers-Tiffée, J. Power Sources 279 (2015) 428–438, https://doi.org/10.1016/j.jpowsour.2015.01.046.
[9] N. Legrand, B. Knosp, P. Desprez, F. Lapicque, S. Raël, J. Power Sources 245 (2014) 208–216, https://doi.org/10.1016/j.jpowsour.2013.06.130.
[10] J.E. Harlow, S.L. Glazier, J. Li, J.R. Dahn, J. Electrochem Soc. 165 (2018) A3595–A3601, https://doi.org/10.1149/2.0011816jes.
[11] M. Ecker, P. Shafiei Sabet, D.U. Sauer, Appl. Energy 206 (2017) 934–946, https://doi.org/10.1016/j.apenergy.2017.08.034.
[12] Z. Li, J. Huang, B. Yann Liaw, V. Metzler, J. Zhang, J. Power Sources 254 (2014) 168–182, https://doi.org/10.1016/j.jpowsour.2013.12.099.
[13] S.F. Schuster, T. Bach, E. Fleder, J. Müller, M. Brand, G. Sextl, A. Jossen, J. Energy Storage 1 (2015) 44–53, https://doi.org/10.1016/j.est.2015.05.003.
[14] C. von Lüders, V. Zinth, S.V. Erhard, P.J. Osswald, M. Hofmann, R. Gilles, A. Jossen, J. Power Sources 342 (2017) 17–23, https://doi.org/10.1016/j.jpowsour.2016.12.032.
[15] T.L. Kulova, A.M. Skundin, E.A. Nizhnikovskii, A.V. Fesenko, Russ. J. Electrochem. 42 (2006) 259–262, https://doi.org/10.1134/S1023193506030086.
[16] U.R. Koleti, T.N.M. Bui, T.Q. Dinh, J. Marco, J. Energy Storage 39 (2021), https://doi.org/10.1016/j.est.2021.102573.
[17] J. Duan, X. Tang, H. Dai, Y. Yang, W. Wu, X. Wei, Y. Huang, Electrochem. Energy Rev. 3 (2020), https://doi.org/10.1007/s41918-019-00060-4.
[18] X. Hu, Y. Zheng, D.A. Howey, H. Perez, A. Foley, M. Pecht, Prog. Energy Combust. Sci. 77 (2020), https://doi.org/10.1016/j.pecs.2019.100806.
[19] C. Uhlmann, J. Illig, M. Ender, R. Schuster, E. Ivers-Tiffée, J. Power Sources 279 (2015) 428–438, https://doi.org/10.1016/j.jpowsour.2015.01.046.
[20] S. Schindler, M. Bauer, M. Petzl, M.A. Danzer, J. Power Sources 304 (2016) 170–180, https://doi.org/10.1016/j.jpowsour.2015.11.044.
[21] D. Anseán, M. Dubarry, A. Devie, B.Y. Liaw, V.M. García, J.C. Viera, M. González, Operando lithium plating quantification and early detection of a commercial LiFePO4 cell cycled under dynamic driving schedule, J. Power Sources 356 (2017) 36–46, https://doi.org/10.1016/j.jpowsour.2017.04.072.
[22] Y. Chen, L. Torres-Castro, K.H. Chen, D. Penley, J. Lamb, M. Karulkar, N. P. Dasgupta, J. Power Sources 539 (2022), https://doi.org/10.1016/j.jpowsour.2022.231601.
[23] M. Koseoglou, E. Tsioumas, D. Ferentinou, I. Panagiotidis, N. Jabbour, D. Papagiannis, C. Mademlis, J. Energy Storage 54 (2022), https://doi.org/10.1016/j.est.2022.105345.
[24] M. Ecker, P. Shafiei Sabet, D.U. Sauer, Appl. Energy 206 (2017) 934–946, https://doi.org/10.1016/j.apenergy.2017.08.034.
[25] C. Uhlmann, J. Illig, M. Ender, R. Schuster, E. Ivers-Tiffée, J. Power Sources 279 (2015) 428–438, https://doi.org/10.1016/j.jpowsour.2015.01.046.
[26] V. Zinth, C. Von Lüders, M. Hofmann, J. Hattendorff, I. Buchberger, S. Erhard, J. Rebelo-Kornmeier, A. Jossen, R. Gilles, J. Power Sources 271 (2014) 152–159, https://doi.org/10.1016/j.jpowsour.2014.07.168.
[27] S. Schindler, M. Bauer, M. Petzl, M.A. Danzer, J. Power Sources 304 (2016) 170–180, https://doi.org/10.1016/j.jpowsour.2015.11.044.
[28] A.K. Padhi, K.S. Nanjundaswamy, J.B. Goodenough, J. Electrochem Soc. 144 (1997) 1188–1194, https://doi.org/10.1149/1.1837571.

[29] M. Petzl, M.A. Danzer, J. Power Sources 254 (2014) 80–87, https://doi.org/10.1016/j.jpowsour.2013.12.060.
[30] Sony Energy Devices Corporation, Lithium Ion Rechargeable Battery Technical Information Model US18650V3, 2011.
[31] D. Lu, M. Scott Trimboli, G. Fan, Y. Wang, G.L. Plett, J. Electrochem Soc. 169 (2022) 080504, https://doi.org/10.1149/1945-7111/ac824a.
[32] Y. Li, M. Abdel-Monem, R. Gopalakrishnan, M. Berecibar, E. Nanini-Maury, N. Omar, P. van den Bossche, J. Van Mierlo, J. Power Sources 373 (2018) 40–53, https://doi.org/10.1016/j.jpowsour.2017.10.092.
[33] B. Epding, B. Rumberg, H. Jahnke, I. Stradtmann, A. Kwade, J. Energy Storage 22 (2019) 249–256, https://doi.org/10.1016/j.est.2019.02.015.
[34] A.J. Smith, P. Svens, M. Varini, G. Lindbergh, R.W. Lindström, J. Electrochem Soc. 168 (2021) 110530, https://doi.org/10.1149/1945-7111/ac2d17.
[35] M. Dubarry, C. Truchot, M. Cugnet, B.Y. Liaw, K. Gering, S. Sazhin, D. Jamison, C. Michelbacher, J. Power Sources 196 (2011) 10328–10335, https://doi.org/10.1016/j.jpowsour.2011.08.077.
[36] Michael Heß, Kinetics and stage transitions of graphite for lithium-ion batteries, ETH Zurich, 2013.
[37] V. Laue, F. Röder, U. Krewer, J. Appl. Electrochem 51 (2021) 1253–1265, https://doi.org/10.1007/s10800-021-01579-5.